AAA Workshop Series Volume 14

Asociación Argentina de Astronomía

Massive Stars and Interacting Binaries
Proceedings of the 1st Padova - Buenos Aires Workshop

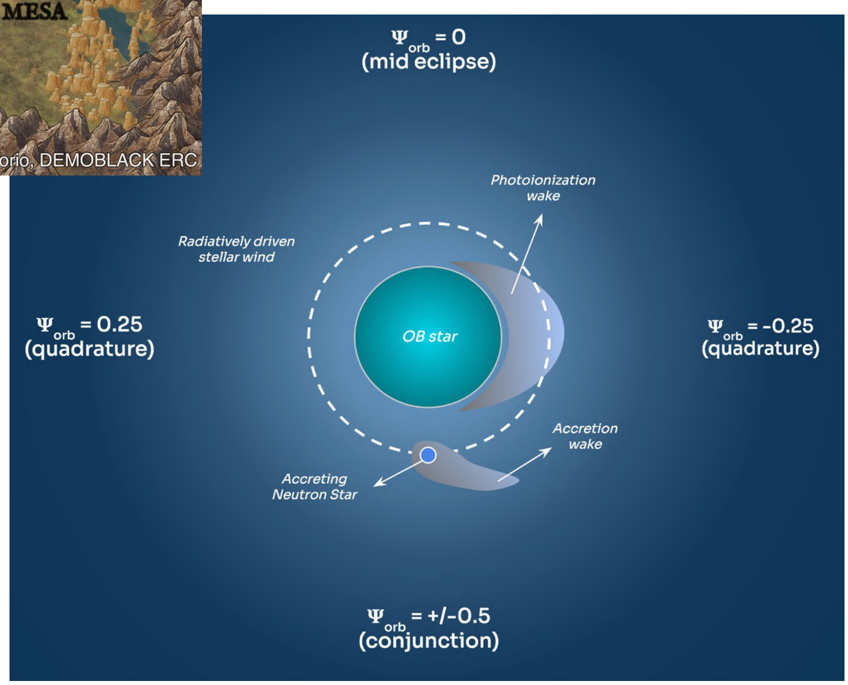

Buenos Aires, Argentina

April 29 - May 3, 2024

Asociación Argentina de Astronomía

Massive Stars and Interacting Binaries
Proceedings of the 1st Padova-Buenos Aires Workshop

Buenos Aires, Argentina, April 29–May 3, 2024

L.J. Pellizza, G.J. Escobar, S.E. Pedrosa, S.E. Nuza, eds.

Credits

Cover:

Top left:
The landscape of population synthesis codes (Iorio & Escobar, pp. 15–20).

Bottom right:
Stellar wind environment leading to asymmetric eclipses in an X-ray binary (Fogantini et al., pp. 51–54).

Massive stars and interacting binaries : proceedings of the 1st Padova-Buenos Aires Workshop /
Editado por Leonardo Pellizza ... [et al.]. - 1a ed. - La Plata : Asociación Argentina de Astronomía, 2026.
Libro digital, PDF - (AAA Workshop Series ; 14)

Archivo Digital: descarga y online
ISBN 978-987-24948-9-6

1. Astrofísica. 2. Estrellas. I. Pellizza, Leonardo, ed. II. Título.
CDD 523.1

Asociación Argentina de Astronomía

Fundada en 1958

Personería Jurídica (Legajo 21.459 - Matr. 1.421), Pcia. de Buenos Aires

Asociación Argentina de Astronomía

Massive Stars and Interacting Binaries
Proceedings of the 1st Padova-Buenos Aires Workshop

Buenos Aires, Argentina, April 29–May 3, 2024

Scientific Organizing Committee

Chair: G.J. Escobar (Università degli studi di Padova)
Members: G. Iorio (Università degli studi di Padova)
S.E. Pedrosa (Instituto de Astronomía y Física del Espacio)
L.J. Pellizza (Instituto de Astronomía y Física del Espacio)

Local Organizing Committee

Chair: L.J. Pellizza (Instituto de Astronomía y Física del Espacio)
Members: M.B. Badaracco (Instituto de Astronomía y Física del Espacio)
L.A. Bignone (Instituto de Astronomía y Física del Espacio)
L. Carvalho (Instituto de Astronomía y Física del Espacio)
P.A. Cataldi (Instituto de Astronomía y Física del Espacio)

Editorial Committee

Members: Leonardo J. Pellizza
Gastón J. Escobar
Susana E. Pedrosa
Sebastián E. Nuza

Sponsors

Foreword

The understanding of the properties, formation and evolutionary channels of stellar systems comprising high-mass stars is currently at the forefront of Astrophysics. Massive stars are luminous sources of electromagnetic radiation that produce powerful massive outflows. At the end of their lives they explode as supernovae, injecting large amounts of energy into their surroundings. Those evolving in binary systems may become also luminous sources of high-energy radiation powered by accretion, and launch relativistic jets. The influence of high-mass stars in their medium is therefore strong, and occurs during their brief lifetimes, which modifies their neighborhood in a significant way.

Among other effects, these stars are responsible for the heating and ionization of the intergalactic medium at the Cosmic Dawn, the regulation of star formation in galaxies, and the chemical evolution of the Universe. High-mass stellar remnants (neutron stars, black holes) are also interesting in their own right because they may be used to test the physics on extreme conditions, such as very dense matter or intense gravitational fields. The investigation of the latter is particularly timely, given the new window to the Universe opened recently by gravitational-wave observatories.

Population synthesis is a technique developed in the last two decades, which combines the latest results on stellar evolution with the power of state-of-the-art computational resources to predict the properties of large groups of stars and binaries at any time in their evolution. It allows therefore to explore the observable properties of these systems, compare to actual observations, validate evolutionary theories, and investigate how they affect the systems in which they live.

The First Padova-Buenos Aires Workshop on Massive Stars and Interacting Binaries (`ganegroup.github.io/workshop/Workshop_on_Massive_stars`) was successfully held in Buenos Aires, Argentina between April 29 and May 4, 2024. It was organized by the Group of Numerical and Extragalactic Astrophysics (GANE, `https://ganegroup.github.io/`) at the Institute for Astronomy and Space Physics (CONICET/UBA, Argentina) and members of the DEMOBLACK group at the University of Padova (UniPD, Italy). The aim was to bring together researchers working in binary population synthesis at Padova University with colleagues in Argentina interested in using these techniques. The main goal was to foster collaborations between groups, discussing possible joint programs to investigate high-mass stellar and binary populations and their effects on diverse systems in the Universe.

The meeting was attended by 56 participants from Argentina, Italy, Chile, France, Germany, Spain, and the United Kingdom. A relaxed program with 11 senior plenary speakers, 23 contributed talks and plenty of time for discussion was prepared. The contributions presented, of which this volume includes a good sample, covered a variety of fields in massive-stars and interacting binaries research: stellar and binary populations, models and hydrodynamic simulations, the relation to galaxies and their environment, and observational counterparts.

The Workshop organization was sponsored by the National Council for Scientific and Technical Research (CONICET), the Argentine Astronomical Society (AAA), the Universities of Padova (UniPD) and Buenos Aires (UBA), and the Institute for Astronomy and Space Physics (CONICET/UBA). We are grateful to all these organizations.

We are indebted to the reviewers of the papers published in this volume, who helped to improve the manuscripts. We especially thank the members of the Local Organizing Committee, and the students who helped with the organization.

Leonardo J. Pellizza
Gastón J. Escobar
Susana E. Pedrosa
Sebastián E. Nuza

Conference picture.

Contents

Invited contributions

Asociación Argentina de Astronomía
Massive Stars and Interacting Binaries: 1st Padova–Buenos Aires Workshop
AAA Workshop Series 14, 2026
L.J. Pellizza, G.J. Escobar, S.E. Pedrosa & S.E. Nuza, eds.

Computing stellar evolution in binary systems

O.G. Benvenuto[1,2]

[1]*Facultad de Ciencias Astronómicas y Geofísicas, UNLP, Argentina*
[2]*Instituto de Astrofísica de La Plata (IALP), Argentina*

Abstract. We describe the main characteristics of a computer code designed to calculate the evolution of stars in close binary systems that may undergo mass transfer episodes. We pay special attention to the strategy we employ to find the mass transfer rate between the components and to the numerical stability of these procedures.

1. Introduction

It is well known that a large fraction of the stars belong to binary systems. Because of this fact, studying stellar evolution in this context is of fundamental importance. The essential difference between the evolution of single stars and those in binary systems is that the presence of a companion imposes a maximum size (the Roche lobe) stars can attain, keeping their structure in hydrostatic equilibrium. Swelling beyond it leads to the onset of mass transfer.

This paper briefly describes the main characteristics of the code we developed for modeling binary evolution. The original version of the code has been presented in Benvenuto and De Vito (2003; BDV03).

The remainder of this paper is organized as follows: In Sect. 2 we describe the main characteristics of our code. In Sect. 3 we enumerate the main applications we have made. Finally, in Sect. 4 we describe the future developments to be included.

2. The Binary Evolution Code

Here we describe the main characteristics of our code. It has two parts: one is the solution of the structure of the stars and the mass transfer rate, if any; the other is related to the chemical evolution of their interiors due to nuclear reactions and mixing. The code does not consider the effects of rotation on the structure and chemical evolution of the stars yet.

In the chemical part of the code, we consider a nuclear reaction network including ^{1}H, ^{2}H, ^{3}He, ^{4}He, ^{7}Li, ^{7}Be, ^{12}C, ^{13}C, ^{14}N, ^{15}N, ^{16}O, ^{17}O, ^{18}O, ^{19}F, ^{20}Ne, ^{24}Mg, and ^{28}Si connected by 34 reactions carefully selected among the most relevant ones. We employ a fully implicit finite difference algorithm to solve the resulting set of *stiff* differential equations. Mixing by convection and semiconvection is considered as in Langer, et al. (1985) while thermohaline mixing is treated as in Maeder, et al. (2013). From here on, we shall concentrate mainly on the technique we employ to solve the structure of the stars and their orbit during their evolution. For the case of detached configurations, in which stars are treated as isolated objects, we refer the reader to Kippenhahn, et al. (1967; KWH67).

The equations of stellar evolution as a function of mass (Lagrangian formulation) are (see, e.g., Kippenhahn and Weigert 1990)

$$\frac{\partial P}{\partial m} = -\frac{Gm}{4\pi r^4}, \quad \frac{\partial r}{\partial m} = \frac{1}{4\pi r^2 \rho}, \quad \frac{\partial l}{\partial m} = \varepsilon_{\rm nuc} - \varepsilon_\nu - T\frac{\partial S}{\partial t}\bigg|_m, \tag{1}$$

$$\frac{\partial T}{\partial m} = -\frac{3}{64\pi^2 a_{\rm rad} c}\frac{\kappa l}{T^3 r^4}, \quad \frac{\partial T}{\partial m} = \nabla_{\rm conv}\frac{T}{P}\frac{\partial P}{\partial m}. \tag{2}$$

These are the equation of hydrostatic equilibrium, the radius embraced by a shell of mass width dm, the conservation of energy, and the energy transport that gives the radiative or convective (Eq. 2 left and right respectively) temperature gradient. The meaning of the quantities is standard. The independent variables are the mass m embraced by a sphere of radius r and the time t. The dependent ones are the pressure P, r, the luminosity l, and the temperature T. The other quantities are the gravitational constant G, the density ρ, the energy release due to nuclear reactions $\varepsilon_{\rm nuc}$, the losses due to neutrino emission ε_ν, S is the entropy, κ is the opacity (radiative and conductive), $a_{\rm rad}$ is the constant of radiation, c is the speed of light, and $\nabla_{\rm conv}$ is the convective gradient, provided by a theory of convection, usually the mixing length theory. We employ the Schwarzschild criterion of convection. Notice that the temporal derivative of the entropy is taken for a fixed mass element. As usual, we denote the mass, luminosity, and radius of the star with M, L, and R respectively. The effective temperature $T_{\rm eff}$ fulfills the usual relation $L = 4\pi R^2 \sigma T_{\rm eff}^4$, where σ is the Stefan-Boltzmann constant.

Apart from the standard equations of stellar evolution, we have to add those specifically corresponding to binary evolution. The size of the Roche lobe as a function of the orbital semiaxis a is given by $R_{\rm L}/a = 0.49q^{1/3}/\big(0.6q^{2/3} + \ln(1+q^{1/3})\big)$ (Eggleton 1983) where $R_{\rm L}$ is the radius of a sphere having the same volume as the actual Roche Lobe, and $q \equiv M_1/M_2$ is the mass ratio of the pair. Subindex 1 (2) corresponds to the donor (accretor) star.

The mass transfer rate is given by $\dot{M} = \dot{M}_0 \ \exp\big((R - R_{\rm L})/H_p\big)$ (Ritter 1988). Here, $\dot{M}_0$ is the mass transfer rate for a star that just fills its lobe. It is a smooth function of the main characteristics of the donor star (for further details, see Ritter 1988), and $H_p \equiv -dr/d\ln p$ is the pressure scale height at the donor's photosphere. The semiaxis evolution is given by

$$\frac{1}{a}\frac{da}{dt} = \frac{2}{J}\frac{dJ}{dt} + \dot{M}_1\left(\frac{1}{M_1+M_2} - \frac{2}{M_1}\right) + \dot{M}_2\left(\frac{1}{M_1+M_2} - \frac{2}{M_2}\right) \tag{3}$$

Here, dJ/dt represents the angular momentum (AM) losses, which may be due to non-conservative mass transfer, gravitational radiation, and magnetic braking. Usually, it is assumed that $\dot{M}_2 = -\beta\dot{M}_1$, where β ($0 \leq \beta \leq 1$) is considered as a fixed free parameter. Notice that $\beta = 1$ (0) corresponds to conservative (fully non-conservative) mass transfer. In the case of non-conservative mass transfer, another parameter α is included, which represents the specific AM of the lost material measured in units of the specific AM of the companion star $dJ/dt\|_{\rm ml} = -\alpha\big(1-\beta\big)a_2^2\omega\dot{M}_1$. Here, ω is the orbital angular velocity and a_2 is the distance of the companion star to the center of mass of the system. Also, it is necessary to add prescriptions for AM losses due to magnetic braking and gravitational radiation

In the present version of the code, the AM corresponding to the rotation of each star is neglected. This formulation assumes instantaneous synchronization between stellar and orbital rotation. If we relax this approximation we would need to consider the tidal evolution of the system.

It is convenient to employ the change of variable $m = M\big(1-e^{\xi}\big)$ and divide the star into several concentric spherical layers, with their surfaces defined at mesh points (typically up to a few thousand) denoted by $\xi_i, \quad i = 1, \cdots, N$. If the pair is semidetached, a mass transfer episode is ongoing. To compute an evolutionary step for the donor star, we need to find its internal structure and the mass transfer rate; and consequently, the mass of the components and the semiaxis of the orbit. We devised a fully implicit, generalized "Henyey" scheme to ensure good numerical stability. Then, $\dot{M}$ has to be iterated simultaneously with the values of L, $T_{\rm eff}$ and p_i, r_i, l_i, and T_i at each mesh point. Let us remark that $\dot{M}$ is *not a local variable*, but affects the whole model since $M = M^{\rm prev} + \dot{M}\Delta t$, where Δt is the timestep between consecutive models. We have to compute the corrections for each variable by solving a huge matrix equation. This is possible since p_i, r_i, l_i, and T_i are local and, as a consequence, the matrix is diagonal in blocks. In the case of mass transfer, the matrix has a non-zero column. This shows the need for a generalization of the standard algorithm presented in KWH67. The lack of space prevents us from presenting here the full matrix algorithm; we refer the reader to BDV03.

When the mass transfer occurs, one needs to be careful in computing the temporal derivative of the entropy. It is taken at constant m; so, we must consider the change in ξ by

$$\frac{\partial S}{\partial t}\bigg|_m = \frac{\partial S}{\partial t}\bigg|_\xi + \frac{\partial S}{\partial \xi}\bigg|_t \frac{\partial \xi}{\partial t}\bigg|_m. \tag{4}$$

Since they are positive, it is convenient to change p, r, and T to logarithmic variables (denoted by $\tilde{p}$, $\tilde{r}$, and $\tilde{T}$ respectively). l may be negative; so, it has to be treated linearly. There are infinite ways to write the system of equations in finite differences. The most simple is to locate the dependent variables l_i, $\tilde{p}_i$, $\tilde{r}_i$, $\tilde{T}_i$ at each point (as done by KWH67). This is simple but prone to undergo numerical instability when computing fast evolutionary stages like those of massive stars beyond helium core exhaustion. A better strategy is to locate *extensive variables* (radius, mass, and luminosity) at each mesh point whereas the *intensive variables* (pressure and temperature) are defined in the middle of two consecutive ones. Doing so provides a largely improved numerical stability.

It is of key relevance to compute not the quantities (l_i, $\tilde{p}_i$, $\tilde{r}_i$, $\tilde{T}_i$) but the differences with respect to the previous model (δl_i, $\delta\tilde{p}_i$, $\delta\tilde{x}_i$, $\delta\tilde{T}_i$). To do so, we modify the logarithmic variables as $\psi_i = \psi_i^{\rm prev} + \ln\big(1+\delta\psi_i\big)$ (where ψ is any of them), and for the luminosity we employ $l_i = l_i^{\rm prev} + \delta l_i$. In this way, we avoid subtraction of very similar numbers. This allows the computation of accurate temporal derivatives, with the obvious improvement of the global behavior of the code.

We handle outer boundary conditions assuming rectangle triangles in the L vs. $T_{\rm eff}$ as in KWH67 but for two different values of $\dot{M}_i$ $i = 1, 2$ bracketing the value of $\dot{M}$ corresponding to the model. Thus, neglecting the amount of heat stored in these layers, (i.e., setting the term $\big(\partial S/\partial t\big)\|_\xi$ to zero) allows us to write a system of four ordinary differential equations that are integrated from the photosphere up to the first mesh point of the model (usually embracing a very little portion of the stellar mass). An interpolation in L, $T_{\rm eff}$, and $\dot{M}_i$ provides the desired boundary conditions.

The beginning and end of the mass transfer process are found automatically. In all cases, we compare the size of the star with that of the Roche lobe. If the star is swelling, we assume the onset of the mass transfer if $(R - R_{\rm L})/H_p > -15$. On the contrary, if the star is contracting, the end of mass transfer occurs when $(R - R_{\rm L})/H_p < -18$. The difference between these thresholds (-15 and -18) is important to avoid spurious oscillations between detachment and semi-detachment stages.

During mass transfer, the chemical profile of the donor star moves outwards. This should be simulated carefully since it can vary very steeply, e.g., during advanced shell burning. Usually, we perform it by employing the method of interpolation presented by Steffen (1990).

In the case of, e.g., Low Mass X-ray Binaries (LMXBs) we compute the donor evolution solely. In these systems, the companion is a neutron star (NS). So, we do not evolve the structure of the NS, but only consider its mass growth. If we are also interested in the evolution of the accreting component of the pair (e.g., in the case of blue straggler stars), we compute the detailed structure of this star considering the effects due to the mass received from the donor. This can be easily solved by assuming the same strategy as for the donor during mass transfer and considering the inwards migration of the chemical profile. On the top of the star, the material coming from the companion is accumulated. Such material can have a molecular weight higher than that of the underlying layers, leading to thermohaline mixing.

3. Some applications of the Code

Here we shall present some applications of our code to objects of particular astrophysical interest.

Perhaps, one of the objects for which it is most difficult to simulate its evolution is LMXBs in which irradiation feedback is considered (Büning and Ritter 2004). When the donor undergoes mass transfer, the material falling onto the NS produces X-ray emission. Part of this radiation illuminates a portion of the donor. The flux of energy $F_{\rm irr}$ received by the donor is given by $F_{\rm irr} = (\alpha_{\rm irr}/4\pi a^2)(GM_2/R_2)$ where $\alpha_{\rm irr}$ is a parameter describing that the energy may not be fully released as X-rays and may not be isotropic.

Suppose that the outer layers of the donor star are cool enough to have a rather thick outer convective zone. In that case, the incoming irradiation has the effect that the illuminated portion of the photosphere is partially inhibited from releasing energy from the stellar interior. This may lead to the occurrence

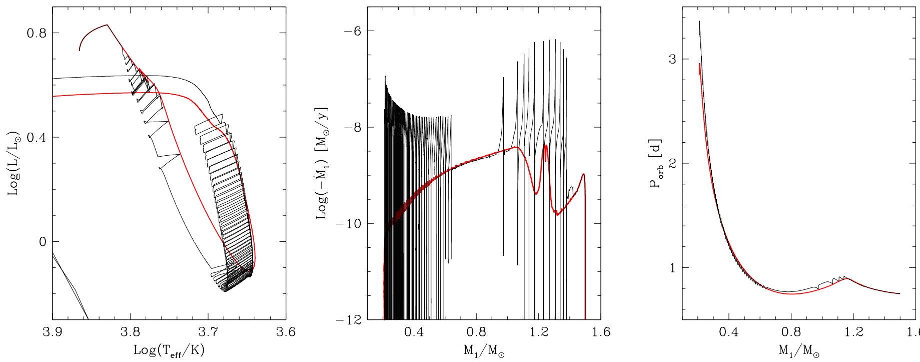

Figure 1. The evolution of a system with a solar composition donor of $1.5\,M_\odot$, and an NS of $1.4\,M_\odot$ on an orbit with an initial period of 0.75 d. The red line represents the case without irradiation feedback whereas, the black line depicts the case of an irradiated model with $\alpha_{\rm irrad} = 0.010$. The left panel shows the HR diagram for the donor. The middle panel corresponds to the mass transfer rate. While the model without irradiation undergoes a long-standing mass transfer episode, the irradiated model undergoes several cycles of mass transfer and detachment. The right panel depicts the evolution of the orbital period in both cases. These are remarkably similar.

of a large number of mass transfer episodes in place of a long, continuous one; see, e.g., Benvenuto, et al. (2014).

In the left panel of Fig. 1 we show the Hertzsprung-Russell (HR) diagram for an LMXB system of a solar composition donor of $1.5\,M_\odot$, and an NS of $1.4\,M_\odot$ on an orbit with an initial period of 0.75 d. In the case of non-irradiated models, the mass transfer occurs in a single, long-standing episode. Quite on the contrary, irradiated models undergo a sequence of mass transfer and detachments (middle panel). Despite this, the evolution of the orbital period, shown in the right panel, is very similar. In any case, there is a fundamental difference between these treatments. If irradiation feedback is considered, when detached, the system should be detected as a binary millisecond pulsar at conditions at which, in the frame of non-irradiated models we would expect to see an LMXB.

The lack of space prevents us from giving a detailed description of other applications that have already been performed. So, we give some general remarks and refer the reader to the respective publication. Our code has also been applied to perform an exploration of different magnetic braking prescriptions and the formation of Ultra Compact X-ray binaries (Echeveste, et al. 2024). In Rain, et al. (2024) we studied the formation of blue and yellow straggler stars. Normal donors with black hole companions have been studied in Bartolomeo Koninckx, et al. (2023). We have arrived at the interesting result that the spin regime of the black hole in V404 Cyg cannot be attained only through mass transfer in the binary. In Novarino, et al. (2021) we studied the time derivative of the orbital period of a millisecond pulsar. Also, for the case of massive binaries, we have computed the pre-supernova evolution of systems to find a progenitor of SN 2011dh (Benvenuto, et al. 2013). Our calculations indicate that a system with $16\,M_\odot + 10\,M_\odot$ with an initial period of 125 days is a plausible progenitor of the explosion.

4. Conclusions

In this paper, we presented a general description of the code we employ for simulating the evolution of stars belonging to binary systems. This tool is modified permanently to keep it up to date. Among the most important improvements to be performed soon, we plan to include rotation. Also, a new, more detailed nuclear reaction network will be included.

Acknowledgements. The author thanks the Organizing Committee of the 1st Padova-Buenos Aires Workshop on Massive Stars and Interacting Binaries, and especially to Dr. Gastón Escobar for inviting him to present this talk. Also, he wants to thank the members of the "Grupo de Evolución de Sistemas BInarios" (GESBI) and especially to Dra. María Alejandra De Vito for years of collaboration. He is a Member of the Carrera del Investigador Científico of the Comisión de Investigaciones Científicas de la Provincia de Buenos Aires.

References

Bartolomeo Koninckx, L., De Vito, M.A., Benvenuto, O.G. 2023, A&A, 674, A97

Benvenuto, O.G., De Vito, M.A. 2003, MNRAS, 342, 50 (BDV03)

Benvenuto, O.G., Bersten, M.C., Nomoto, K. 2013, ApJ, 762, 74

Benvenuto, O.G., De Vito, M.A., Horvath, J.E. 2014, ApJ, 786, L7

Büning, A., Ritter, H. 2004, A&A, 423, 281

Echeveste, M., et al. 2020, MNRAS, 495, 2509

Echeveste, M., et al. 2024,MNRAS, 530, 4277

Eggleton, P.P. 1983, ApJ, 268, 368

Kippenhahn, R., Weigert, A., Hofmeister, E. 1967, Methods in Computational Physics, 7, 129 (KWH67)

Kippenhahn, R., Weigert, A. 1990, "Stellar Structure, Evolution", Springer-Verlag

Langer, N., El Eid, M.F., Fricke, K.J. 1985, A&A, 145, 179-191

Maeder, A., et al. 2013, A&A, 553, A1

Novarino, M.L., et al. 2021, MNRAS, 508, 3812

Rain, M.J., et al. 2024, A&A, 685, A33

Ritter, H. 1988, A&A, 202, 93

Steffen, M. 1990, A&A, 239, 443

Asociación Argentina de Astronomía
Massive Stars and Interacting Binaries: 1st Padova–Buenos Aires Workshop
AAA Workshop Series 14, 2026
L.J. Pellizza, G.J. Escobar, S.E. Pedrosa & S.E. Nuza, eds.

Close binary evolution: brief review, some results and future perspectives

M.A. De Vito[1,2]

[1]*Instituto de Astrofísica de La Plata (IALP), Argentina*
[2]*Facultad de Ciencias Astronómicas y Geofísicas, UNLP, Argentina*

Abstract. The study of binaries is an important topic in astrophysics. A particular and interesting group is that of close binary systems. In these pairs, the stars are close enough to allow mass transfer between the components during their lifetime. In this contribution, I will briefly review the modeling of close binary systems over the past decades and present some results from our research group.

1. Introduction

It is usual to find stars in groups, such as stellar clusters, associations, and binary systems. The estimated binary fraction ranges from $40\% - 60\%$ for stars with masses around $\sim 1\,\mathrm{M}_\odot$, to nearly 100% for massive A/B and O type stars. This is not surprising, as star formation does not occur in isolation.

In binary systems, almost any combination is possible: different masses, chemical compositions, and evolutionary stages of the components, as well as different orbital periods. The study of binaries is important because, in some cases, it is possible to determine one of the most important parameters that characterize a star: its mass. Moreover, binary systems provide the framework for some of the most interesting astrophysical scenarios, such as the solution of the Algol paradox, the formation of low-mass helium white dwarfs, the recycling of millisecond pulsars, cataclysmic variables, Type Ia supernovae formation, the merger of black holes and neutron stars, among others. All these scenarios have something in common: close binary evolution.

This paper is organized as follows: in Sect. 2, I provide a brief historical review of the development of close binary calculations. In Sect. 3, I present some results obtained by our research group GESBi (Grupo de Evolución en Sistemas Binarios). In Sect. 4, I summarize the main aspects of this contribution.

2. Brief historical review

References to close binary systems (CBSs) date back to the late 19th century, particularly in the context of variable stars. In 1938, Zděnek Kopal studied the orbit of close binaries (Kopal 1938). Since then, numerous researchers have investigated CBSs from both observational and dynamical perspectives. The first calculation of an evolutionary track for the components of a CBS was performed in the pioneering work of Bohdan Paczyński (Paczyński 1966). In 1967, B. Paczyński published a series of papers studying various cases of close binary (CB) evolution. He first considered conservative evolution, where neither mass nor angular momentum is lost from the system. In collaboration with Janusz Ziołkowski, he explored the effects of mass loss from the system. Later, he presented a code employing the Henyey method and studied the emission of gravitational waves in the context of CBSs (Paczyński 1967). In 1969, J. Ziołkowski published his results on the formation of Algol-type systems in CBSs (Ziołkowski 1969).

The calculation of the evolution of a CBS requires an estimate of an important quantity: the Roche lobe radius, $R_{\rm L}$. The Roche lobe of a star is defined in the framework of the restricted three-body problem (see, e.g., Moulton 1970). Consider two main bodies (the components of a binary) with masses M_1 and M_2, and a third component with a very small mass compared to the others. Under the assumption of circular orbits, with the stellar rotation synchronized with the orbital motion, and in the reference frame co-rotating with the binary, we can write the gravitational potential and find the equipotential surfaces. The most important of these surfaces is the one enclosing each star, known as *the Roche lobe*. These lobes touch at the inner Lagrangian point L_1. A representative value for the radius of the Roche lobe was estimated by P. Eggleton (Eggleton 1983) considering a sphere with an equivalent volume of the Roche lobe

$$\frac{R_{\rm L,1}}{a} = \frac{0.49q^{2/3}}{0.6q^{2/3} + \ln(1 + q^{1/3})}, \qquad (1)$$

where $R_{\rm L,1}$ is the radius of the Roche lobe of the star with mass M_1, and the mass ratio is defined as $q = M_1/M_2$[1].

Once a component of a CBS fills its Roche lobe (when its radius R equals $R_{\rm L}$), a mass transfer episode begins. We refer to this component as the *donor*. The evolution of the stars becomes completely different from what they would have been if they were isolated (or in a wide, detached-binary, where $R < R_{\rm L}$ always).

Kippenhahn & Weigert (1967) introduced different cases of mass transfer depending on the evolutionary stage of the donor star at the onset of mass transfer, that is, on when the donor star fills its Roche lobe: Case A, during core hydrogen burning; Case B, after the exhaustion of core hydrogen but before the onset of core helium burning; and Case C, after the onset of core helium burning.

Over the following decades, many authors devoted significant effort to calculating the evolution of CBs and improving numerical models. A. V. Tutukov & L. R. Yungelson (Tutukov & Yungelson 1971) began investigating the effects of mass and angular momentum losses from the system. E. P. J. van den Heuvel & C. De Loore (van den Heuvel & De Loore 1973) linked the evolution of CBSs with an accreting neutron star (NS) in an X-ray emission source (such as Cygnus X-3). I. Iben & A. Tutukov (Iben & Tutukov 1984a) included the effects of gravitational radiation and magnetic winds in CB evolution. In the same year, they published a paper (Iben & Tutukov 1984b) studying the formation of a Type Ia supernova as the end product of the evolution of binaries with components of moderate initial mass. P. C. Joss, Ph. Podsiadlowski, J. J. L. Hsu & S. Rappaport (Joss et al. 1988) presented models that account for Supernova 1987A as originating

[1]To calculate $R_{\rm L,2}$ we must replace q with q^{-1} in Eq. 1.

from a stripped asymptotic giant branch star in a CBS. Many other studies were carried out in the early 2000s, including those by Han, Tout & Eggleton (2000) and Podsiadlowski, Rappaport & Pfahl (2002). With the advent of the publicly available MESA code (Modules for Experiments in Stellar Astrophysics; Paxton et al. 2011), an increasing number of researchers have conducted studies of CB evolution.

3. Some results

3.1. Our first calculations

In 2003, we published the first version of our code for calculating the evolution of CBSs (Benvenuto & De Vito 2003). The code calculates the detailed evolution of the donor star in a CBS from the Zero-Age Main Sequence (ZAMS) to its final evolutionary stage (in this case a low-mass helium white dwarf). The main characteristic of our code is that the mass transfer rate is included as an additional variable in the system of stellar structure and evolution equations, while the orbital evolution is followed simultaneously. The code allows for both conservative and non-conservative calculations. In that paper, we presented, for the first time, results obtained with our code for the evolution of three binary systems. Two of them, with an initial mass $M_{\mathrm{d,i}} = 2.0\,\mathrm{M}_\odot$, an initial mass ratio $q_{\mathrm{i}} = 1.5$, and initial orbital periods $P_{\mathrm{orb,i}}$ of 1.5 (MODEL I) and 0.7 d (MODEL II); the third system had initial parameters $M_{\mathrm{d,i}} = 1.4\,\mathrm{M}_\odot$, $q_{\mathrm{i}} = 1.0$ and $P_{\mathrm{orb,i}} = 1.0\,\mathrm{d}$ (MODEL III). In these calculations, it was assumed that all the mass lost by the donor star leaves the system, (no accretion onto the accreting component), and that half of the specific angular momentum is carried away by the lost material.

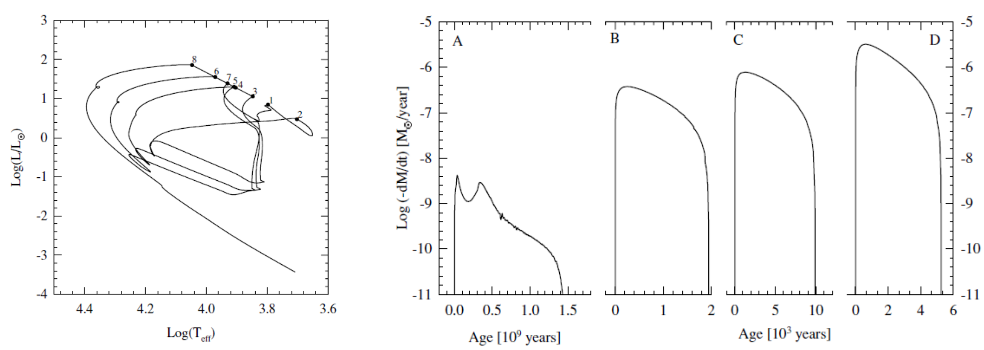

Figure 1. Evolutionary track of the donor star corresponding to MODEL III (left) and mass-loss rate from this component (right). Taken from Benvenuto & De Vito (2003), Figs. 7 and 8.

As an example, I describe MODEL III. The left panel of Fig. 1 shows the evolutionary track of the donor star, while the right panel shows the evolution of the mass-loss rate of this component. As can be seen, this track is completely different from that of an isolated 1.4 $M_\odot$ star. In the case of a donor in a CBS, the crossing of the Hertzsprung gap toward lower effective temperatures is prevented by the donor filling its Roche lobe (point 1), and the first mass-transfer episode begins. The luminosity drops abruptly, and the star loses almost 85 % of its

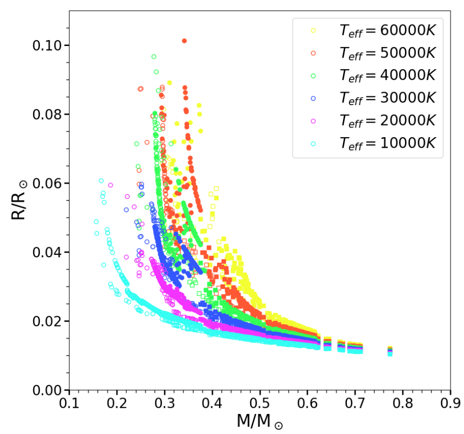

Figure 2. The MRR obtained for WDs resulting from CBSs evolution. Colors corresponds to different values of the effective temperature on the cooling track.

mass. This is the longest episode, ending at point 2 after almost 1.5×10^9 years (see A, in the right panel of Fig. 1). The orbital period of the binary nearly triples its initial value, increasing to $P_{\rm orb} = 2.8$ d. The occurrence of three thermonuclear flashes causes the donor to expand, leading to three additional mass-loss episodes. However, these episodes are so short that neither the donor mass nor the orbital period changes significantly. The donor ends its evolution as a helium white dwarf with a mass of $\sim 0.2\,{\rm M}_\odot$. For a detailed description of Models I, II, and III, the reader is referred to Benvenuto & De Vito (2003).

3.2. The mass–radius relation for white dwarfs resulting from CBSs

One of the most important factors affecting the mass–radius relation (MRR) of white dwarfs (WDs) is the hydrogen content of their envelopes. This problem was studied, among others, by Romero et al. (2019). They employed a set of single stellar evolution models of carbon–oxygen core WD sequences with masses between 0.493 and $1.05\,{\rm M}_\odot$. Motivated by this, in Pereiras (2023) we designed a grid of calculations with the aim of obtaining a MRR for WDs coming from CBSs. These models consist of main-sequence donor stars that evolve into WDs, accompanied by an accreting NS or black hole (BH). The initial parameters considered were

- for $M_{\rm NS,i} = 1.4\,{\rm M}_\odot$: $M_{\rm d,i}$ from 0.5 to $10\,{\rm M}_\odot$, and $P_{\rm orb,i}$ from 0.5 to 2.5 d;
- for $M_{\rm BH,i} = 4, 6, 8, 10\,{\rm M}_\odot$: $M_{\rm d,i}$ from 0.75 to $10\,{\rm M}_\odot$, and $P_{\rm orb,i}$ from 1 to 8 d.

The calculations were performed under non-conservative conditions, assuming solar metallicity for the donor stars and no irradiation feedback.

The MRR obtained from these models is presented in Fig. 2. The colors correspond to different values of the effective temperature along the cooling track. Note that the MRR is wider at higher effective temperatures. This is because the remnant of the donor retains memory of its previous binary evolution at the beginning of the cooling track, through the hydrogen content in its envelope. Moreover, the lower the mass of the remnant, the broader the MRR. As effective temperature decreases, this dispersion gradually disappears. While the MRR presented by Romero et al. (2019) covers WD masses between 0.5 and $1\,\mathrm{M}_\odot$, Pereiras (2023) extends it to much lower WD masses, down to $\sim 0.2\,\mathrm{M}_\odot$.

3.3. Cataclysmic variables from close binary evolution

Cataclysmic variables (CVs) are CBSs composed of a normal low-mass star and an accreting WD. We began studying this class of systems with two main objectives:

(i) to identify a possible progenitor of SS Cyg,
(ii) to find possible progenitors of CVs with accurately determined characteristic parameters, such as the masses of the components and the orbital period.

These results were presented in Rodriguez (2024).

(i) The SS Cyg system consists of a donor star with a mass of $M = 0.59\,\mathrm{M}_\odot$, an effective temperature of $T_{\mathrm{eff}} = 4750\,\mathrm{K}$, and a radius of $R = 0.6^{+0.03}_{-0.01}\,\mathrm{R}_\odot$. The accreting WD has a mass of $0.91\,\mathrm{M}_\odot$, and the binary has an orbital period of $P_{\mathrm{orb}} = 0.2751\,\mathrm{d}$. The estimated mass-loss rate from the donor is $\dot{M} = (1.4 - 6.4) \times 10^{-9}\,\mathrm{M}_\odot\,\mathrm{yr}^{-1}$, and the mass ratio is $q = 0.628$.

To identify a possible progenitor of SS Cyg, we designed a grid of calculations of CBSs. The best candidate for reproducing the current characteristic parameters of SS Cyg was a system initially composed of a $1.0\,\mathrm{M}_\odot$ donor star and a $0.9\,\mathrm{M}_\odot$ accreting WD in a 0.375 d orbit. This system reproduces all the current parameters of SS Cyg, as shown in Fig. 3.

(ii) Following our study of SS Cyg, we extended the calculations to other CVs. We searched for possible progenitors of ten CVs. However, since the range of possible WD masses is wider than that of NSs, we found more than one possible progenitor for some systems. This result motivates a more detailed study in the future.

4. Conclusions and future perspectives

In this contribution, a brief historical overview of CB evolution calculations was presented. In addition, some results obtained by our research group from modeling close binary evolution in different frameworks were discussed. As GESBi can perform detailed calculations of CBSs in different contexts, we hope that our models will be useful for applications in population synthesis studies.

Acknowledgements. I would like to thank the organizers of this workshop for inviting me to present this contribution and for their efforts in making this amazing and productive meeting possible.

References

Benvenuto O.G., De Vito M.A. 2003, MNRAS, 342, 50
Chandrasekhar S. 1931, ApJ, 74, 81

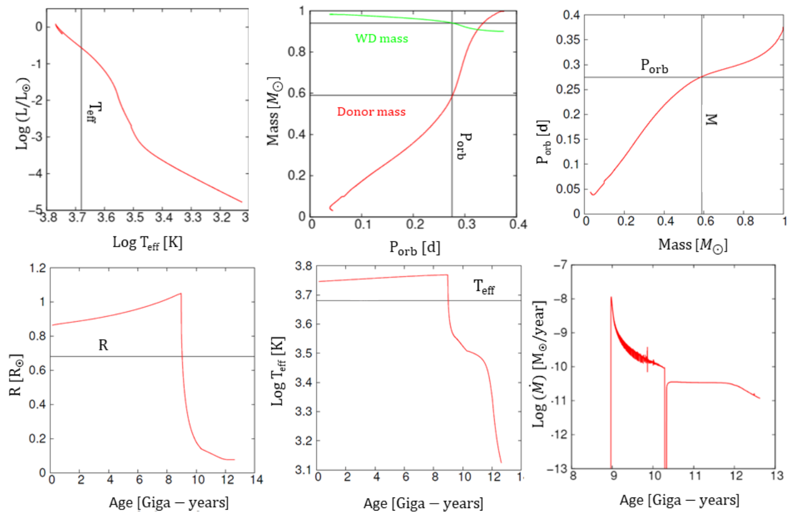

Figure 3. Fit of the SS Cyg parameters obtained from our progenitor. Black lines indicate the observed values of the effective temperature ($T_{\rm eff}$), mass (M), and radius (R) of the donor star, as well as the orbital period ($P_{\rm orb}$) of the system.

Eggleton P.P. 1983, ApJ, 268, 368
Han Z., Tout C.A., Eggleton P.P. 2000, MNRAS, 319, 215
Iben I., Tutukov A.V. 1984a, ApJ, 284, 719
Iben I., Tutukov A.V. 1984b, ApJS, 54, 335
Joss P.C., et al. 1988, Nature, 331, 237
Kippenhahn R., Weigert A. 1967, ZA, 65, 251
Kopal Z. 1938, MNRAS, 98, 448
Moulton F.R. 1914, "An Introduction to Celestial Mechanics", Macmillan
Paczyński B. 1966, AcA, 16, 231
Paczyński B. 1967, AcA, 17, 287
Paxton B., et al. 2011, ApJS, 192, 3
Pereiras R.H., Tesis de Licenciatura 2023, https://sedici.unlp.edu.ar/handle/10915/151124
Podsiadlowski P., Rappaport S., Pfahl E.D. 2002, ApJ, 565, 1107
Rodriguez C., Tesis de Licenciatura 2024, https://sedici.unlp.edu.ar/handle/10915/165142
Romero A.D., et al. 2019, MNRAS, 484, 2711
Tremblay P.-E., et al. 2017, MNRAS, 465, 2849
Tutukov A.V., Yungelson L.R. 1971, NInfo, 20, 86
van den Heuvel E.P.J., De Loore C. 1973, A&A, 25, 387
Ziołkowski J. 1969, ASSL, 13, 231

Asociación Argentina de Astronomía
Massive Stars and Interacting Binaries: 1st Padova–Buenos Aires Workshop
AAA Workshop Series 14, 2026
L.J. Pellizza, G.J. Escobar, S.E. Pedrosa & S.E. Nuza, eds.

SEVN and its friends: present and future of population synthesis codes

G. Iorio[1,2], G.J. Escobar[3,4]

[1] *Institut de Ciències del Cosmos, Universitat de Barcelona, Spain*
[2] *Università degli studi di Padova, Italia*
[3] *Instituto de Astrofísica de Canarias, España*
[4] *Universidad de La Laguna, Tenerife, España*

Abstract. Rapid population synthesis codes (PSCs) are the standard tool to study the evolution of large stellar and binary populations and their outcomes, from gravitational-wave mergers to X-ray binaries and peculiar transients. We review the current landscape of PSCs, focusing on the difference between codes based on analytic fitting formulas and those based on the interpolation of pre-computed stellar tracks. We then present SEVN, a track-interpolation PSC, describing its recent updates, its growing ecosystem of tools (the SEVN$_{\rm py}$ Python module, the SEVNweb browser application), and some representative applications. Finally, we discuss the improvements needed to exploit the wealth of data expected in the coming years, when the increasing statistics of electromagnetic and gravitational-wave observations will make model systematics the dominant source of uncertainty.

1. Introduction

Most massive stars are members of binary or higher-order multiple systems (e.g. Offner et al. 2023), and a large fraction of them interact with a companion during their lifetime through tides, mass transfer, and common envelope episodes. Binary interactions shape some of the most interesting phenomena in modern astrophysics: gravitational-wave mergers, X-ray binaries, dormant black hole–star systems, peculiar transients, and exotic stellar populations. Studying these outcomes requires simulating the evolution of millions to billions of stars and binaries, a task beyond the reach of detailed stellar evolution codes and hydrodynamical simulations. Rapid PSCs fill this gap, evolving large stellar populations in minutes to hours by means of analytic, semi-analytic, or interpolation-based prescriptions. We review the current landscape of PSCs (Sect. 2), introduce SEVN, its recent updates and main applications (Sect. 3), and discuss the improvements needed to fully exploit the forthcoming wealth of observational data (Sect. 4).

2. The current landscape of population synthesis codes

In recent years, a wide variety of PSCs has flourished, many of which are publicly available, regularly maintained, and supported by an established user community. This wealth of tools is a valuable resource for the community, both because each code has its own speciality and because it allows us to investigate the systematics introduced by different assumptions and methods in the study of stellar populations. Fig. 1 presents a chart of this landscape: rivers represent

Figure 1. A schematic overview of the current state of the art of PSCs. The map is an oversimplification for the sake of visualisation.

detailed stellar evolution codes (e.g. STARS, Eggleton et al. 2011; MESA, Paxton et al. 2011; PARSEC, Bressan et al. 2012), while cities and ships symbolize PSCs. The position of each code reflects the stellar evolution models it relies upon. The full list of codes and references is available in the associated repository (doi.org/10.5281/zenodo.13923596); here we focus on the main families.

The most populated region of the map is the BSE island, which hosts the descendants of the original BSE code (Hurley et al. 2002). These codes describe single stellar evolution by analytic fitting formulas (Hurley et al. 2000) calibrated on the stellar tracks of Pols et al. (1998), computed with the code STARS. This approach is extremely fast and numerically robust, and it has enabled a large fraction of the population synthesis results of the last two decades, but the underlying stellar physics is essentially frozen to the state of the art of the late 1990s: the original tracks were computed without stellar winds (added a posteriori) and cover a limited range of masses (0.5–50 $M_{\odot}$) and metallicities ($0.0001 < Z < 0.03$). Modern implementations update the wind prescriptions and extend the parameter range, but changing the underlying stellar models would require a complete re-derivation of the fitting formulas.

The Interpolators Lake gathers the codes that follow a different strategy: instead of fitting formulas, single stellar evolution is obtained by interpolating sets of pre-computed stellar tracks (METISSE, Agrawal et al. 2020; SEVN, Iorio et al. 2023). In principle, these codes are not tied to any specific stellar evolution code: any set of tracks can be loaded, provided it is converted to the required table format. This decouples the stellar evolution models from the binary evolution prescriptions, and makes the choice of the stellar physics an explicit, easily explorable dimension of the parameter space, which constitutes the key advantage over fitting-formula codes, at the cost of a heavier memory footprint and of the need to pre-compute complete sets of tracks.

Finally, the ships in the map represent hybrid approaches that bridge detailed stellar and binary evolution with population synthesis: the Brussels code (De Donder & Vanbeveren 2004), BPASS (Eldridge et al. 2017), and POSYDON (Fragos et al. 2023). In particular, POSYDON interpolates grids of full MESA binary models, retaining the self-consistency of detailed binary calculations at the price of very large pre-computed grids, which must be recomputed whenever the stellar or binary physics parameters are changed.

3. The SEVN population synthesis code

SEVN (Stellar EVolution for N-body) belongs to the family of track-interpolation codes: its first version was presented in Spera et al. (2019), while the current public one is described in Iorio et al. (2023). Single stellar evolution is computed through the interpolation of pre-computed tables derived from stellar tracks, both for hydrogen-rich stars and for stripped stars with a bare helium core. Tables are loaded at runtime, making the exploration of different stellar evolution models straightforward: changing the underlying stellar physics does not require any recompilation of the code, but simply the selection of a different set of tables.

Following the idea of the original BSE code, binary evolution and the formation and evolution of compact remnants are implemented through analytic and semi-analytic prescriptions. Binary processes include wind mass accretion, Roche-lobe overflow, stellar tides, common envelope, gravitational-wave orbital decay, and the orbital modifications due to supernova kicks. One of the key aspects of SEVN is the adaptive time step. During stellar and binary evolution, the next integration step is predicted from the current relative variations of the stellar and binary properties, and a step is repeated whenever a property changes by more than a given tolerance. As a result, the time steps naturally adapt to the evolutionary phase, ranging from a few months during the fast interaction phases to $\sim$Myr during quiescent evolution, guaranteeing both accuracy and speed.

The details of the implemented prescriptions and of the interpolation scheme can be found in Iorio et al. (2023). Here we report the most relevant updates included in the current main version (gitlab.com/sevncodes/sevn/-/tree/v2.17.4): (i) a new formalism for the maximum efficiency of wind mass accretion based on the model by Tejeda & Toala (2025); (ii) a new default natal-kick distribution based on the log-normal distribution by Disberg & Mandel (2025); (iii) a more self-consistent treatment of the critical mass ratio for mass-transfer stability, presented in Echeveste et al. (2026), which accounts for the effects of the actual (in general non-conservative) accretion efficiency.

3.1. The SEVN framework

Since its first versions, SEVN has grown both in terms of tools and community. In addition to the standard C++ executables that can be used to evolve a list of stars and binaries, SEVN can be used as a library to embed stellar and binary evolution in C++ and Python codes. In particular, we have recently released SEVN_{py} (sevn.readthedocs.io/en/latest), a module for SEVN that includes both utilities to handle the SEVN output and built-in tools to evolve stars and binaries directly from Python, while relying on the fast and efficient C++ SEVN library as a backend. The set of tools is completed by SEVNweb, a web application that runs SEVN directly in the browser (through a WebAssembly port of the code). In addition to a new landing page (sevncodes.gitlab.io/sevn), we have created a Zenodo community repository (zenodo.org/communities/sevn) containing stellar tables, input and output data to reproduce published results obtained with SEVN, tutorials, and presentations. The most updated sets of tables are also available on Zenodo. Further new sets of tables can be generated from any stellar evolution code with the publicly available code TRACKCRUNCHER (gitlab.com/sevncodes/trackcruncher), so that the collection of available models is expected to keep growing together with the SEVN community.

3.2. Science with SEVN

SEVN, like the other interpolating PSCs, is particularly valuable for massive stars and binaries, where the large uncertainties in stellar models, winds, and final fates, combined with the lack of calibrators, make stellar evolution an additional, fundamental dimension of the parameter space to be explored together with binary processes. A clear example, taken from Iorio et al. (2023), is shown in Fig. 2: using SEVN with PARSEC tracks and the standard Hurley et al. (2002) mass-transfer stability criteria, the merger efficiency of binary neutron stars decreases with metallicity, in contrast with the flat trend commonly found by BSE-like codes (e.g. van Son et al. 2025). The difference is driven purely by stellar evolution: in the Hurley et al. (2002) tracks, neutron star progenitors at high metallicity ignite core-helium burning while still compact, whereas in PARSEC they do so after a considerable expansion, so that the second interaction with the companion becomes an unstable mass transfer ending in a merger, suppressing the formation of tight binary neutron stars. The flat trend is recovered only by forcing all mass transfer from donors with a radiative envelope to be stable. Uncertainties in massive-star evolution correlate with the choice of binary evolution parameters, thus a comprehensive exploration of both dimensions is essential.

SEVN has been used extensively to investigate the demography of binary compact objects (e.g. Iorio et al. 2023; Sgalletta et al. 2025; Korb et al. 2025). Beyond these, the coupling of SEVN with the GALAXEV spectral evolution code (Bruzual & Charlot 2003) has been used to model the nebular emission of young stellar populations including binary products (Lecroq et al. 2024), while SEVN with MIST tracks has been used to show that Gaia BH3, a non-interacting binary hosting a $\sim$33 $\mathrm{M}_\odot$ black hole and a low-mass, very metal-poor companion, is a common outcome of isolated binary evolution at low metallicity (Iorio et al. 2024). SEVN has also been coupled with cosmological simulations to follow the evolution of binary compact objects across cosmic time (Marinacci et al. 2026). Finally, SEVN is designed as a library for easy coupling with N-body codes, and it has already been interfaced with the new BIFROST code (Rantala et al. 2025).

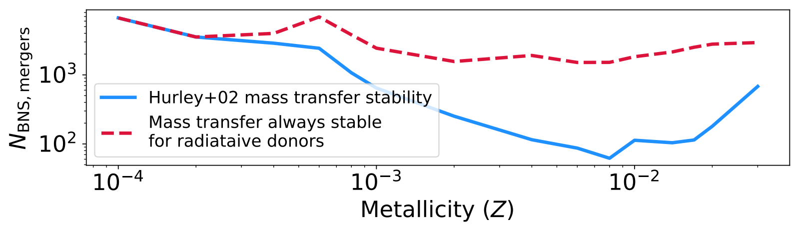

Figure 2. Differences in the predicted number of binary neutron stars merging within a Hubble time as a function of metallicity, obtained with different mass-transfer stability criteria. Data from Iorio et al. (2023).

4. Future improvements and conclusions

PSCs are also starting to show tensions with observations, especially concerning more massive stars. The predicted merger rates of binary black holes tend to be overestimated, and the discrepancy grows as the metal-dependent star formation history is modelled more accurately (e.g. Sgalletta et al. 2025; Marinacci et al. 2026), while isolated binary evolution with standard assumptions struggles to reproduce the dormant black hole binaries like Gaia BH1 and BH2 (e.g. Olejak et al. 2026; Mapelli et al. 2026). Most of these studies point toward a revision of the same few critical ingredients: common envelope evolution, mass-transfer stability, and the supernova models and natal kicks. The wealth of data expected in the coming years, from electromagnetic surveys and Gaia DR4 to third-generation gravitational-wave detectors, will drastically reduce the statistical uncertainties, leaving model systematics as the dominant limitation. Most of the theoretical work must be done along these three main lines: (i) A better description of the common envelope. The classical $\alpha\lambda$ formalism is oversimplified and likely overoptimistic about common envelope survival. Alternative models have already been proposed (e.g. Trani et al. 2022; Hirai & Mandel 2022; Di Stefano et al. 2023) and must be implemented and tested in population synthesis, but hydrodynamical simulations are still far from convergence (e.g. the review by Schneider 2025), and more work on the underlying astrophysical model is needed. (ii) A revision of the mass-transfer stability criteria: the standard critical mass ratios depend only on the evolutionary phase of the donor and assume conservative mass transfer, while detailed calculations indicate a more complex behaviour (e.g. Ge et al. 2020; Klencki et al. 2026). (iii) Updated supernova and natal-kick prescriptions, together with a more self-consistent treatment of the evolution of stars affected by binary interactions, integrating detailed models of binary-stripped stars (e.g. Laplace et al. 2021), the interpolation of full binary grids already implemented in POSYDON (Fragos et al. 2023), or the interpolation of tracks including mass accretion and mass loss, currently under development in SEVN. The improvement of PSCs, in synergy with targeted modelling performed with detailed codes such as MESA, will be fundamental to decode the astrophysics of stellar and binary evolution imprinted in the incredible wealth of data expected in the near future.

Acknowledgements. SEVN has been made possible thanks to European Research Council Consolidator grant DEMOBLACK (contract no. 770017). GI (and SEVN maintenance) is supported by La Caixa Foundation fellowship grant ID 100010434, code LCF/BQ/PI24/12040020. GI acknowledges support under the National Recovery and Resilience Plan (NRRP), Mission 4, Component 2, Investment 1.4, Call for tender No.3138 of 18/12/2021 of Italian Ministry of University and Research funded by the European Union-NextGenerationEU. GJE acknowledges support by the Spanish Ministry of Science via Plan de Generación de Conocimiento grant PID2022-143331NB-100. Authors acknowledge financial support from the Consorzio interUniversitario Italiano per l'Argentina (CUIA).

References

Agrawal, A. et al. 2020, ApJ, 904, 169
Bressan, A. et al. 2012, MNRAS, 427, 127
Bruzual, G., Charlot, S. 2003, MNRAS, 344, 1000
De Donder, E., Vanbeveren, D. 2004, New Astronomy, 9, 1
Di Stefano, R. et al. 2023, ApJ, 944, 87
Disberg, P., Mandel, I. 2025, ApJ, 989, 8
Echeveste, M. et al. 2026, arXiv:2606.30303
Eggleton, P.P. et al. 2011, Astrophysics Source Code Library, ascl:1107.008
Eldridge, J.J. et al. 2017, PASA, 34, 58
Fragos, T. et al., 2023, ApJS, 264, 45
Ge, H. et al. 2020, ApJS, 249, 9
Hirai, R., Mandel, I. 2022, ApJ, 937, 42
Hurley, J. et al. 2000, MNRAS, 315, 543; 2002, MNRAS, 329, 897
Iorio, G. et al. 2023, MNRAS, 524, 426; 2024, A&A, 690, 144
Klencki, J. et al. 2026, A&A, 706, 296
Korb, E. et al. 2025, A&A, 695, 199
Laplace, E. et al. 2021, A&A, 656, 58
Lecroq, M. et al. 2024, MNRAS, 527, 9480
Mapelli, M. et al. 2026, arXiv:2604.12839
Marinacci, F. et al. 2026, A&A, 707, 140
Offner, S.S.R. et al. 2023, ASPC, 534, 275
Olejak, A. et al. 2026, ApJ, 1006, 13
Paxton, B. et al. 2011, ApJS, 192, 3
Pols, O. et al. 1998, MNRAS, 298, 525
Rantala, A. et al. 2025, MNRAS, 543, 2130
Schneider, F.R.N. 2025, arXiv:2509.18421
Sgalletta, C. et al. 2025, A&A, 698, 144
Spera, M. et al. 2019, MNRAS, 485, 889
Tejeda, E., Toalá, J.A. 2025, ApJ, 980, 226
Trani, A.A. et al. 2022, PhRvD, 106, 3014
van Son, L.A.C. et al. 2025, ApJ, 979, 209

Oral contributions

Asociación Argentina de Astronomía
Massive Stars and Interacting Binaries: 1st Padova–Buenos Aires Workshop
AAA Workshop Series 14, 2026
L.J. Pellizza, G.J. Escobar, S.E. Pedrosa & S.E. Nuza, eds.

The nature of the coronal regions in ultraluminous X-ray sources

L. Abaroa[1,2], G.E. Romero[1,2], L.M. Pasquevich[2]

[1]*Instituto Argentino de Radioastronomía (IAR)*
[2]*Facultad de Ciencias Astronómicas y Geofísicas, UNLP, Argentina*

Abstract. Ultraluminous X-ray sources (ULXs) are accreting astrophysical objects whose X-ray luminosity appears to be higher than the Eddington luminosity. The emission of ULXs is dominated by the thermal component of the innermost region of the accretion disk. However, in some ULXs the radiation extends to energies above 10 keV, which cannot be produced in the disk. This hard X-ray emission requires an additional nonthermal component, which may originate in a coronal-like region. The origin of such a region is still unclear. In this paper we discuss how electrons and protons can be injected and accelerated in these systems to produce the observed spectra.

1. Introduction

One of the main features of a black hole (BH) accreting at super-Eddington rates is the ejection of powerful winds from its accretion disk (e.g., Shakura & Sunyaev 1973; Fukue 2004). These winds have a conical geometry near the black hole (Abaroa et al. 2023, Abaroa & Romero 2024b) and obscure most of the thermal emission from the disk (Abaroa et al. 2024a,b). In the case of stellar-mass BHs in binary systems, the wind can interact with the companion star, leading to the formation of shocks (Abaroa et al. 2021), while in the case of supermassive BHs the wind interacts with all objects orbiting the galactic center (e.g., Sotomayor & Romero 2022, Abaroa & Romero 2024a).

Ultraluminous X-ray sources (ULXs) are thought to be accreting X-ray binaries with a super-Eddington compact stellar-mass object (such as a BH). A beaming effect could be responsible for the observed X-ray luminosity (King 2010): the radiation emitted from the inner part of the accretion disk is geometrically collimated by the ejected wind, which is optically thick except for a narrow channel or funnel around the black hole axis.

Most ULX spectra show a combination of a thermal blackbody component and a power-law component. The former corresponds to the inner hot accretion disk, while the latter is thought to be caused by Comptonization of the soft photons by relativistic electrons in the magnetocentrifugal funnel formed by the wind walls (e.g. Combi et al. 2024). An open question is how the electrons in this funnel are accelerated to form these coronal Comptonizing regions in ULXs. Here we present a preliminary characterization of the acceleration region in the funnel of these systems. Extended results on this topic can be found in Romero et al. (2026).

2. Model

2.1. Disk and wind

We assume that the compact object in the binary system is a stellar-mass BH of mass $M_{\rm BH} = 10\,M_\odot$ accreting matter at super-Eddington rates ($\dot{M}_{\rm input} > \dot{M}_{\rm Edd}$) from an evolved massive star. The Eddington rate is given by

$$\dot{M}_{\rm Edd} = \frac{L_{\rm Edd}}{\eta c^2} \approx 2.2 \times 10^{-8} M_{\rm BH}\,{\rm yr}^{-1} = 1.4 \times 10^{18} \frac{M_{\rm BH}}{M_\odot}\,{\rm g\,s}^{-1}, \quad (1)$$

where $L_{\rm Edd}$ is the Eddington luminosity, $\eta \approx 0.1$ the accretion efficiency, and c the speed of light. The disk becomes geometrically thick in its inner region, where the ejection of winds by the radiation force helps to regulate the mass accretion rate to the BH ($\dot{M}_{\rm acc}$) at the Eddington rate. Such regulation results in a total mass loss rate in winds $\dot{M}_{\rm w}$ that is approximately equal to the accretion input, $\dot{M}_{\rm w} \approx \dot{M}_{\rm input}$.

The effects of the radiation on the matter at the escape surface of the disk in the inner region have been calculated in detail by Abaroa et al. (2023). The radiation field transfers both energy and angular momentum to the wind, which escapes the system with a strong equatorial component, forming a funnel above the BH (Combi et al. 2024). This scenario is typical for ULXs under the assumption of superaccretion (Fabrika 2021).

Table 1 Parameters of the model.

Parameter	Symbol	Value	Units
Black hole mass	$M_{\rm BH}$	10	$M_\odot$
Eddington accretion rate	$\dot{M}_{\rm Edd}$	2.2×10^{-7}	$M_\odot$ yr^{-1}
Mass accretion rate	$\dot{M}_{\rm input}$	2.2×10^{-6}	$M_\odot$ yr^{-1}
Gas velocity	$v_{\rm gas}$	0.2	c
Funnel semi opening angle	θ	15	degrees
Viewing angle	i	≈ 0	degrees

When the system is oriented face-on (i.e., with an inclination angle of $i \approx 0°$), the only X-ray emission visible from the disk is that which escapes through the funnel, i.e., the emission produced near the innermost part. The dense wind surrounding the low-density channel produces a geometric beaming effect that leads an observer to infer an isotropic bolometric disk luminosity given by $L_{\rm beamed} \approx L_{\rm Edd}[1 + \ln \dot{m}/b]$, where $\dot{m}$ is the normalized accretion rate and $b \sim 73/\dot{m}^2$ is the beaming factor (King 2010). Table 1 shows the relevant parameters used in our model.

2.2. Funnel

We assume that a gas of particles travels at semi-relativistic speeds through the transparent channel formed by the conical wind above the BH. These particles can enter the funnel directly from the innermost disk, where magnetic reconnection and accretion of non-dipolar magnetic fields can produce rapid flares that drag the particles along (see Romero & Gutierrez 2020). The density of this gas must be low enough to guarantee the optically-thin state of the funnel, that is, an observer at infinity must be able to see the radiation from the innermost accretion disk. This implies that the optical depth along the line of sight must be less than unity, $\tau < 1$. The density of the gas in the funnel is given by $\rho_{\rm gas} = \dot{M}_{\rm gas}/\Omega\, z^2\, v_{\rm gas}$, where $\dot{M}_{\rm gas}$ is the mass input to the funnel, Ω is the solid angle of the duct, and z is the height above the BH. We assume the gas velocity is $v_{\rm gas} = 0.2c$, so $\beta_{\rm gas} = 0.2$ and the Lorentz factor is $\gamma_{\rm gas} \approx 1.02$ (Abaroa et al. 2023). We get the condition $\rho_{\rm gas} < 10^{-11}\,{\rm g\,cm^{-3}}$ with the parameters of our model, by solving the integral for the optical depth and imposing the transparency limit mentioned above:

$$\tau = \int_0^\infty \gamma_{\rm gas}(1 - \beta_{\rm gas}\cos i)\,\kappa_{\rm co}\,\rho_{\rm co}{\rm d}z \approx \int_0^\infty \kappa_{\rm co}\,\rho_{\rm co}{\rm d}z < 1, \tag{2}$$

where $\kappa_{\rm co} \approx \kappa$ is the opacity and $\rho_{\rm co} \approx \rho_{\rm gas}$ (the sub-index co refers to the comoving frame).

Shocks in the funnel can accelerate some particles to relativistic energies. Internal shocks occur when the flow is matter-dominated, that is, when the matter energy density is greater than the magnetic energy density, $e_{\rm p}(z) = \dot{M}_{\rm gas}v_{\rm gas}/2\pi z^2 > B^2(z)/8\pi = e_{\rm m}(z)$. The magnetic field near the BH is calculated assuming equipartition between the magnetic and radiative energy densities, $e_{\rm m}(z) = e_{\rm r} = L/\Omega r^2 c$ (with L the luminosity of the radiation field). The magnetic field in the funnel decreases with distance z from the BH, $B(z) = B_0(z'/z)$, where $z' \approx 10\,r_{\rm g}$. On the other hand, the radiative energy density, $e_{\rm r}$, is calculated considering the thermal fields of the disk and the wind photosphere as blackbodies with temperatures of $T_{\rm disk} = 10^7\,{\rm K}$ and $T_{\rm wind} = 10^5\,{\rm K}$, respectively. We find that $e_{\rm p}(z) > e_{\rm m}(z)$ at a height $z_{\rm acc} \sim 5\times10^9\,{\rm cm}$, where we assume particle acceleration occurs and where the magnetic field is $B \approx 10^5\,{\rm G}$. The size of the acceleration region is $\Delta_{\rm acc} = 0.1\,z_{\rm acc}$.

3. Results

Once we determine the location of the coronal region, we calculate the particle acceleration. We assume a diffusive shock mechanism and an advective escape from this region. We calculate synchrotron and inverse Compton (IC) cooling for electrons, and synchrotron, proton-proton, and photo-protonic interactions for protons. The ambient fields for the interactions are the magnetic field described in the previous section, the radiation fields from the disk and the wind photosphere, and the matter density also estimated in the previous section. Fig. 1 shows our results for the energy gain and losses of electrons (left) and protons (right). Electrons cool efficiently by synchrotron and IC, and reach a maximum energy of $\sim$ 10 GeV. Protons cool by photo-meson interactions and reach a maximum energy of $\sim$ 20 TeV.

As can be seen from our results, IC is a relevant cooling process mainly at low energies ($<$ 10 MeV). This Comptonization with the thermal photons from the disk may produce the nonthermal tail at hard X-rays observed in the spectra of some ULXs. On the other hand, proton cooling will be of interest for calculation of the soft γ-rays produced in the funnel (see Romero et al. 2026).

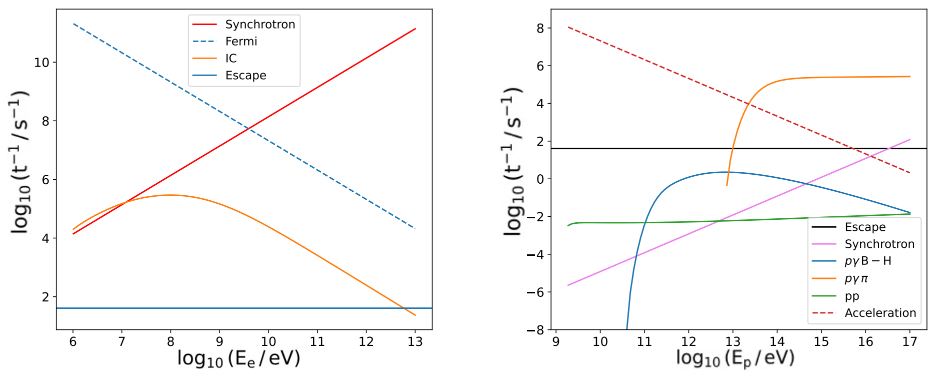

Figure 1. Energy gain and losses of electrons (left) and protons (right). The efficiency of the acceleration is 10^{-2}.

4. Conclusions

We present preliminary results for the energy gain and loss of primary particles in the coronal regions formed in the transparent funnel above the black hole of ULXs. We find that electrons can reach energies of ~ 10 GeV cooling mainly by synchrotron radiation, while protons cool by photo-hadronic interactions reaching energies of ~ 20 TeV. A complete study of the radiative processes of both particle populations will be presented in forthcoming articles.

References

Abaroa, L., Romero, G.E. 2024a, A&A, 691, A73
Abaroa, L., Romero, G.E. 2024b, RMAA Conf. Ser., 56, 39-44
Abaroa, L., et al. 2024a, PoS(HEPRO VIII), 55
Abaroa, L., et al. 2024b, A&A, 691, A93
Abaroa, L., Romero, G.E., Sotomayor, P. 2023, A&A, 671, A9
Abaroa, L., Sotomayor Checa, P., Romero, G.E. 2021, BAAA, 62, 262
Combi, J.A., Fogantini, F.A., Saavedra, E.A., et al. 2024, A&A, 686, A121
Fabrika, S.N., et al. 2021, Astrophys. Bull., 76, 6
Fukue, J. 2004, PASJ, 56, 569
King, A.R. 2010, MNRAS, 402, 1516
Romero, G.E., Gutiérrez, E. 2020, Universe, 6, 99
Romero, G.R., Pasquevich L.M., Abaroa L. 2026, APh 175, id.103173
Shakura, N.I., Sunyaev, R.A. 1973, A&A, 500, 33
Sotomayor, P., Romero, G.E. 2022, A&A, 664, A178

Asociación Argentina de Astronomía
Massive Stars and Interacting Binaries: 1st Padova–Buenos Aires Workshop
AAA Workshop Series 14, 2026
L.J. Pellizza, G.J. Escobar, S.E. Pedrosa & S.E. Nuza, eds.

Dimension reduction techniques applied to Chandra X-ray data

M.B. Badaracco[1], L. Bignone[1], L.J. Pellizza[1], G.J. Escobar[2], S.E. Pedrosa[1]

[1]*Instituto de Astronomía y Física del Espacio (IAFE), Argentina*
[2]*Università degli studi di Padova, Italia*

Abstract. The properties of the first stars formed during the Epoch of Reionization (EoR, $10^8 - 10^9$ yr after the Big Bang) and their influence on galaxy evolution are central to extragalactic astrophysics. High Mass X-ray Binaries (HMXBs) may have contributed significantly to the feedback at that epoch, affecting both cosmic star formation and the ionization of the intergalactic medium (IGM). Their study in the Early Universe can be approached through low-metallicity galaxies at redshift zero, considered local analogs of those at the EoR. A key challenge is distinguishing HMXBs from Low Mass X-ray Binaries (LMXBs) without optical counterparts. Here we apply dimensionality reduction and classification techniques to Chandra data from recent catalogs. Preliminary results show that the most relevant features are hardness ratios and variability, in agreement with previous works.

1. Introduction

It is believed that the EoR began with the birth of the first generations of stars and galaxies, because of their injection of energy into the IGM and interstellar medium (ISM). X-ray binaries have been proposed as important contributors: their radiation could rival the UV emission of massive stars (Power et al. 2009), exceed that of their progenitors and heat the IGM to $\sim 10^4$ K (Mirabel et al. 2011), reduce recombination (Jeon et al. 2014), and significantly heat the ISM through kinetic feedback (Artale et al. 2015). To assess the impact of HMXBs during the EoR, we aim to analyze their properties in local low-metallicity galaxies, considered analogs of early systems. This requires distinguishing HMXBs from LMXBs, which are classified by the donor mass. Positional association with optical counterparts often fails at large distances. Mineo et al. (2012) proposed a spatial method, but restricted to face-on spirals. Alternatively, X-ray features alone may allow classification (van Paradijs 1998), motivating the use of variability and hardness ratios. Machine learning provides a new tool to address such problems. Kumaran et al. (2023) classified point-like X-ray sources with supervised learning, reaching F1 scores[1] $\gtrsim 0.88$, though relying on distance-dependent features and without application to other galaxies. Pérez-Díaz et al.

[1]F1 score is defined as the harmonic mean of the precision and recall. Precision measures the proportion of true positives among all positive predictions for a given class. Recall measures the proportion of instances that are correctly identified as belonging to a given class.

(2024) applied unsupervised methods that separate compact accretors (XRBs and AGN) with confidence but confuse HMXBs and LMXBs. They defined new features from Chandra Source Catalog 2.0, consistent with the criteria above. The present work examines this selection.

2. Procedure

We crossmatched CSC 2.1.1 (Evans et al. 2024) with the catalogs of Fortin et al. (2023, 2024) using the *CDS XMatch Service* (Pineau et al. 2011), obtaining 77 HMXBs and 121 LMXBs. The explored features are listed in Pérez-Díaz et al. (2024, Table 1). Source code is available online[2]. Dimensionality reduction was performed with Principal Component Analysis (PCA) and Uniform Manifold Approximation and Projection (UMAP; McInnes, Healy & Melville 2020). After PCA, the two principal components ($PC1$, $PC2$) were used as covariates in a logistic regression model:

$$P(\text{LMXB}|PC1, PC2) = (1 + e^{-(\alpha+\beta_1 PC1+\beta_2 PC2)})^{-1}, \quad (1)$$

applied to the test set to predict LMXB probabilities (sources with $P < 0.5$ are classified as HMXBs). We also evaluated Random Forest, with and without UMAP preprocessing. In all experiments the random seed was fixed to 42, the reduced space dimension was 2, the test set was 20% of the data, and features were standardized to $N(0, 1)$. For UMAP, we set `n_neighbors`=3, `min_dist`=0, and explored all available metrics[3]. Missing values were treated in two ways: in Experiment 1 (Exp. 1), entries with NaNs were excluded (as in Pérez-Díaz et al. 2024), reducing sample size but avoiding spurious information; in Experiment 2 (Exp. 2), missing values were imputed with the mean of each feature, using only the training set. Accordingly, missing values in the test set were replaced with the corresponding training means to prevent data leakage. The same principle applied to standardization, with the test set scaled using the training mean and variance.

3. Results

In Fig. 1 we show the results of dimensionality reduction and in Fig. 2 the confusion matrices. For Exp. 1, PC1 is dominated by the hardness ratio between hard and soft bands, while for Exp. 2 is dominated by the index of the fitted power law. In both cases, PC2 reflects broadband variability, with some LMXBs standing out as outliers at extreme PC2 values. In both PCA cases, HMXB and LMXB clusters overlap substantially. The logistic regression classifier yields F1 scores for HMXB of 0.61 (Exp. 1) and 0.12 (Exp. 2), as can be obtained from Fig. 2. With UMAP, more clusters and complex patterns appear, though still

---

[2] https://github.com/mbbadaracco/Dimension-reduction-techniques-applied-to-Chandra-X-ray-data

[3] `n_neighbors` balances local vs. global structure, `min_dist` controls cluster compactness, and the metric defines distance in the input space.

overlapping. The best F1 score for HMXB in Exp. 1, 0.708, is obtained with `braycurtis` metric. For Exp. 2 and the same metric, the F1 score for HMXB is 0.473. Despite UMAP reducing computing time by $\sim 10\%$, higher F1 scores are obtained without it: 0.833 (Exp. 1) and 0.575 (Exp. 2).

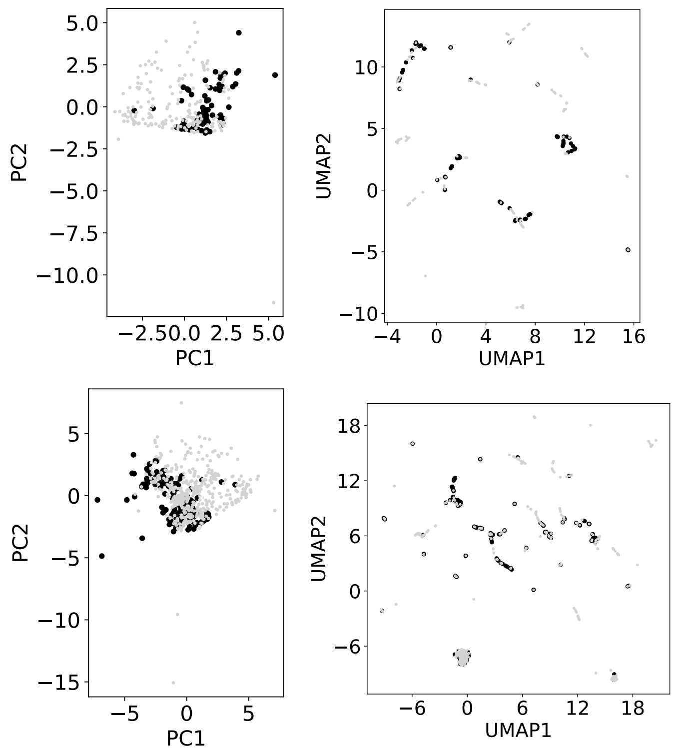

Figure 1. Black dots represent HMXBs and grey dots LMXBs. The upper panels show Exp. 1: left corresponds to clustering with PCA, right to clustering with UMAP using `braycurtis` metric. The lower panels show the same for Experiment 2.

4. Conclusions

This work is a first exploration of dimensionality reduction and classification for X-ray binaries. Results are promising, showing that HMXBs and LMXBs can be distinguished using only X-ray data. Future work includes enlarging the dataset with other X-ray observatories, ensuring homogeneity, and incorporating catalogs of quasars and AGNs. Preprocessing will thus be a valuable tool to reduce the computing time of classification algorithms.

References

Artale M.C., Tissera P.B., Pellizza L.J. 2015, MNRAS, 448, 3071

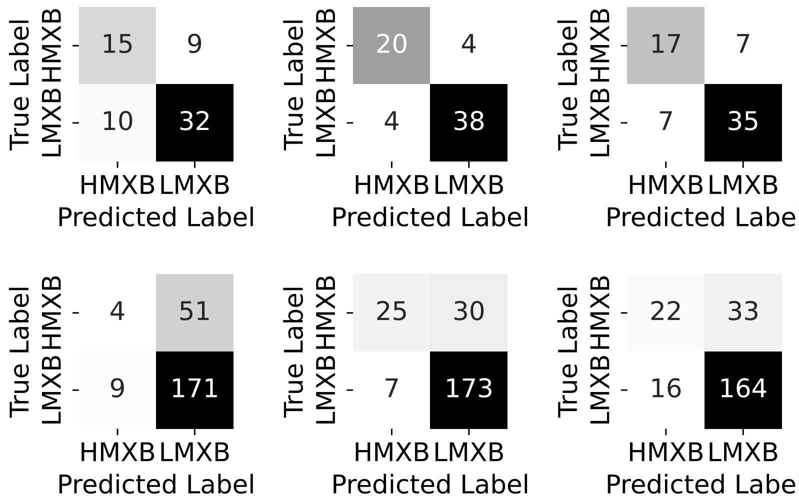

Figure 2. Confusion matrices. The upper panels show Exp. 1, and the lower panels show Exp. 2. Left panels correspond to PCA with logistic regression, middle panels to Random Forest without UMAP preprocessing, and right panels to Random Forest with UMAP preprocessing using `braycurtis` metric.

Evans I.N., et al. 2024, ApJS, 274, 22

Fortin F., et al. 2023, A&A, 671, A149

Fortin F., et al. 2024, A&A, 684, A124

Jeon M., et al. 2014, MNRAS, 440, 3778

Kumaran S., et al. 2023, MNRAS, 520, 5065

McInnes, L., Healy, J., Melville, J. 2020, arXiv:1802.03426v3

Mineo S., Gilfanov M., Sunyaev R. 2012, MNRAS, 419, 2095

Mirabel I.F., et al. 2011, A&A, 528, A149

Pérez-Díaz V.S., et al. 2024, MNRAS, 528, 4852

Pineau F.-X., et al. 2011, A&A, 527, A126

Power C., et al. 2009, MNRAS, 395, 1146

Van Paradijs J. 1998, ASIC, 515, 279

Asociación Argentina de Astronomía
Massive Stars and Interacting Binaries: 1st Padova–Buenos Aires Workshop
AAA Workshop Series 14, 2026
L.J. Pellizza, G.J. Escobar, S.E. Pedrosa & S.E. Nuza, eds.

Spinning into the void: black holes in low-mass interacting binaries

L. Bartolomeo Koninckx[1,2], M.A. De Vito[1,2], O.G. Benvenuto[1,2]

[1]*Instituto de Astrofísica de La Plata (IALP), Argentina*
[2]*Facultad de Ciencias Astronómicas y Geofísicas, UNLP, Argentina*

Abstract.
Both the mass and spin parameters can fully characterize a rotating black hole. In binary systems where these objects interact with stars, observational estimates of these parameters can occasionally be made. Within such systems, the spin of a black hole intensifies as it accretes material from its companion. Consequently, increased accretion leads to a higher spin rate. In this contribution, we present findings concerning two Low-Mass Interacting binary systems, specifically V404 Cyg and XTE J1550-564, where the dimensionless spin parameter of the black hole has been observationally determined. Utilizing our binary evolution code, we established a progenitor for each system, a crucial step toward deciphering the episodes of mass accretion onto the black hole. By assuming an initially non-rotating black hole and incorporating data from mass transfer episodes for our best models, we investigated the evolution of the black hole's spin parameter. Our analysis suggests that there may be aspects of the black hole formation process that elude our current understanding.

1. Introduction

A binary system is referred to as *interactive* when its components are sufficiently close, or one of the stars expands enough, to fill its Roche lobe. In such cases, the material from one star (the donor) can be transferred to its companion (the accretor), initiating a mass transfer episode[1]. A particularly interesting case arises when the accretor is a black hole (BH). These compact objects are fully characterized by their mass and angular momentum. While the mass of a BH can sometimes be determined dynamically, estimating its rotational angular momentum is more challenging, requiring observations of its surroundings. Two leading methods exist to measure the dimensionless BH spin parameter (a^*), each relying on different components of the X-ray spectrum: the Continuum Fitting (CF) (Novikov & Thorne 1973; Page & Thorne 1974), and the Relativistic Reflection (RR) method (Fabian et al. 1989; Laor 1991).

As a BH accretes matter in a binary system, its spin may increase (Bardeen 1970). While it is commonly assumed that the BH's initial rotation is negligible, whether the observed spin parameters of BHs in low-mass X-ray binaries

[1]A mass transfer episode could also happen due to wind mass loss, which will not be addressed on this work due this mechanism is of less importance for low-mass interacting binaries.

(LMXBs) can be explained solely by accretion remains a matter of debate (Fragos & McClintock 2015; Reynolds 2021). To contribute to this discussion, we aim to study the evolution of the BH spin parameter in two LMXBs with confirmed BHs and measured spins: V404 Cyg and XTE J1550-564.

These systems have been extensively studied, and their key properties—such as the donor's and BH's masses, orbital period, and the donor's luminosity and effective temperature—are summarized in Table 1. For V404 Cyg, the donor's metallicity is measured to be twice solar (González Hernández et al. 2011), while solar metallicity is assumed for XTE J1550-564. The mass-loss rate of the donor ($\dot{M}_{\rm d}$) in both systems has been theoretically estimated, with V404 Cyg exhibiting a value of $\langle \dot{M}_{\rm d} \rangle \sim 1.1 \times 10^{-9}$ $M_\odot yr^{-1}$ (Ziółkowski & Zdziarski 2018), and XTE J1550-564, $\sim 9 \times 10^{-11}$ $M_\odot yr^{-1}$ (Orosz et al. 2011). As for the mass accretion rate onto the black hole, Ziółkowski & Zdziarski (2018) concluded that less than 30% of the mass that is being donated must be accreted for V404 Cyg, but we do not have this information for XTE J1550-564. Spin parameter measurements are also available for these systems. For V404 Cyg, Walton et. al.(2017) reported a lower limit of $a^* > 0.92$ using the RR method, while for XTE J1550-564, a value of $a^* = 0.49^{+0.13}_{-0.2}$ was found through a combination of CF and RR methods, making it one of the rare cases where these two approaches agree (Steiner et al. 2011).

Table 1 Observational data for V404 Cyg and XTE J1550-564.

System	Parameter	Value	Error	Unit	Reference
V404 Cyg	$M_{\rm d}$	0.54	± 0.05	$M_\odot$	(1)(2)
	$M_{\rm BH}$	9	$^{+0.2}_{-0.6}$	$M_\odot$	(1)(2)
	$P_{\rm orb}$	6.47	± 0.001	d	(3)
	$L_{\rm d}$	8.7	$^{+1.7}_{-1.4}$	$L_\odot$	(2)(4)
	$T_{\rm eff}$	4274	$^{+116}_{-113}$	K	(2)(4)(5)
XTE J1550-564	$M_{\rm d}$	0.3	± 0.07	$M_\odot$	(6)
	$M_{\rm BH}$	9.1	± 0.61	$M_\odot$	(6)
	$P_{\rm orb}$	1.5420333	± 0.0000024	d	(6)
	$L_{\rm d}$	1.05	$^{+0.6}_{-0.33}$	$L_\odot$	(6)
	$T_{\rm eff}$	4475	± 250	K	(6)

(1) Casares & Charles (1994); (2) Khargharia et al. (2010); (3) Charles et al. (1989); (4) Cox (2000); (5) Ziółkowski & Zdziarski (2018); (6) Orosz et al. (2011).

2. Procedure

The evolution of the dimensionless BH spin parameter can be studied using the formula presented in Podsiadlowski et al. (2003) (adapted from Bardeen 1970), which depends on the initial and current mass of the BH, assuming an initially non-rotating BH. For this purpose, we employed our binary evolution code (Benvenuto & De Vito 2003; De Vito & Benvenuto 2012; Benvenuto et al. 2012) to determine plausible progenitors for the systems under study, assuming that the secondary star begins to evolve on the zero-age main sequence while the BH has already formed. This step is essential for investigating the mass transfer episodes and, consequently, the accretion of mass by the BH.

A candidate progenitor for each system must reproduce all the quantities listed in Table 1 within their respective observational uncertainties. Among the candidates, we select the best model based on its proximity to the observed data. Once the optimal model for each system is identified, we can analyze the mass transfer episodes, providing us with the accreted mass by the BH over time. Using this information, we calculate the evolution of the BH spin parameter.

3. Results

We explored initial values for the donor and BH mass, the orbital period, and the fraction of mass, β, that is accreted by the BH from the donor (considering both conservative and non-conservative mass transfer scenarios). For further details, the reader is referred to the works of Bartolomeo Koninckx et al. (2023, 2025).

The models that best represent each system from within our initial parameters grid were: $M_{\rm d}^0 = 1.5\,{\rm M}_\odot$, $M_{\rm BH}^0 = 9.0\,{\rm M}_\odot$, $P_{\rm orb}^0 = 1.5\,{\rm d}$ and $\beta = 0.3$ with a metallicity of $Z = 0.028$ for V404 Cyg (Model A). For XTE J1550-564, the best model was achieved with $M_{\rm d}^0 = 1.25\,{\rm M}_\odot$, $M_{\rm BH}^0 = 9\,{\rm M}_\odot$, $P_{\rm orb}^0 = 0.65\,{\rm d}$ and $\beta = 0.5$ (Model B). Both models fall within the observational error margins for all considered parameters. The time at which this agreement occurs, providing the estimated age of each system is referred to as $t_{\rm obs}$. Regarding mass transfer

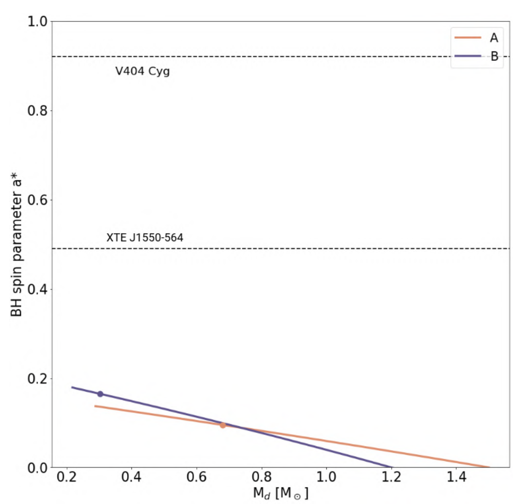

Figure 1. Spin parameter evolution as a function of the donor mass for the models from our grid that best represent the systems V404 Cyg and XTE J1550-564. A dot marks the point where the model reaches $t_{\rm obs}$, and the dashed lines represent the observational estimates for the BH spin parameter in these systems.

episodes, both models show near-perfect agreement with the estimated values at the time $t_{\rm obs}$. We used this data to calculate the BH spin evolution, assuming an initially non-rotating BH. The results are shown in Fig. 1, where for neither system does the evolution of the BH spin parameter reach the observed estimates.

4. Conclusions

We presented plausible progenitors for two LMXB systems: V404 Cyg and XTE J1550-564. Based on the information provided by our models, we studied the evolution of the BH dimensionless spin parameter. Assuming that the initial spin of the BH is negligible, our models were unable to reproduce the observed spin estimates. This challenges the assumption that the BH's initial spin is negligible, suggesting alternative scenarios should be explored.

Acknowledgements. We would like to thank the organizers of the *1st PD-BA Workshop on Massive Stars and Interacting Binaries* for the invitation to present this contributed talk. We also thank the anonymous referee for its constructive comments that helped the manuscript to be clearer.

References

Bardeen J.M. 1970, Nature, 226, 64

Bartolomeo Koninckx L., De Vito M.A., Benvenuto O.G. 2023, A&A, 674, A97

Bartolomeo Koninckx L., De Vito M.A., Benvenuto O.G., 2025, A&A, 703, A126

Benvenuto O.G., De Vito M.A. 2003, MNRAS, 342, 50

Benvenuto O.G., De Vito M.A., Horvath J.E. 2012, ApJ, 753, L33

Casares, J., Charles, P.A. 1994, MNRAS, 271, L5

Charles, P.A., et al. 1989, in ESA Special Publication, Two Topics in X-Ray Astronomy, J. Hunt & B. Battrick eds., p. 103

Cox, A.N. 2000, Allen's astrophysical quantities (Springer Link)

De Vito M.A., Benvenuto O.G. 2012, MNRAS, 421, 2206

Fabian A.C., et al 1989, MNRAS, 238, 729

Fragos T., McClintock J.E. 2015, ApJ, 800, 17

González Hernández, J.I., et al. 2011, ApJ, 738, 95

Khargharia, J., Froning, C.S., Robinson, E.L. 2010, ApJ, 716, 1105

Laor A. 1991, ApJ, 376, 90

Novikov I.D., Thorne K.S. 1973, in Black Holes (Les Astres Occlus), DeWitt C. & DeWitt B. eds., Gordon and Breach, New York, p. 343

Orosz J.A., et al. 2011, ApJ, 730, 75

Page D.N., Thorne K.S. 1974, ApJ, 191, 499

Podsiadlowski P., Rappaport S., Han Z. 2003, MNRAS, 341, 385

Reynolds C.S. 2021, ARA&A, 59, 117

Steiner J.F., et al. 2011, MNRAS, 416, 941

Walton, D.J., et al. 2017, ApJ, 839, 110

Ziółkowski, J., Zdziarski, A.A. 2018, MNRAS, 480, 1580

Asociación Argentina de Astronomía
Massive Stars and Interacting Binaries: 1st Padova–Buenos Aires Workshop
AAA Workshop Series 14, 2026
L.J. Pellizza, G.J. Escobar, S.E. Pedrosa & S.E. Nuza, eds.

Disentangling galaxy morphologies with generative neural networks

L.A. Bignone[1], S.E. Pedrosa[1], L.J. Pellizza[1]

[1]*Instituto de Astronomía y Física del Espacio (IAFE), Argentina*

Abstract. New instruments like the JWST, Euclid, and the Vera Rubin Telescope are extending galaxy observations to unprecedented redshifts and lower surface brightnesses, revealing regions where traditional galaxy morphology taxonomies may no longer apply. At the same time, recent generative AI algorithms have demonstrated a powerful ability to identify and leverage complex relationships within data, particularly in image-based tasks. These models can learn to generate new, realistic images by analysing large datasets. In this work, we introduce the initial elements of an unsupervised galaxy morphology classification method based on Generative Adversarial Networks (GANs), enabling flexible adaptation across various datasets and domains without relying on predefined taxonomies.

1. Introduction

Galaxy morphologies have been typically studied using a variety of parametric and non-parametric methods (Lotz et al. 2004), as well as visual classification. Most of these methods have been devised to study low and intermediate redshift galaxies in the high surface brightness regime. As new instruments such as JWST, Euclid and Vera Rubin reveal galaxies in previously unexplored regions, it becomes very important that we revise the methods and taxonomies we use to classify galaxies so that we can properly link their visual appearance to their physical properties and origin. In recent years, generative neural network models, including Generative Adversarial Networks (GANs, Goodfellow et al. 2014, autoencoders, Kingma & Welling 2019, and diffusion models, Sohl-Dickstein et al. 2015, have made a significant impact across multiple disciplines. These advanced AI algorithms enable the generation of realistic and diverse data samples, fostering advancements in tasks like image synthesis, data augmentation, and style transfer, thereby pushing the boundaries of visual understanding. The power of these models lies in their ability to efficiently capture and organize visual information within images in interpretable and disentangled ways. In this work, we showcase two of the initial components of an unsupervised classification method for galaxy morphology based on GANs deep neural networks. Our approach has been tested on diverse datasets, in this work we present results from deep images from the Hyper Suprime-Cam Subaru Strategic Program (HSC-SSP, Aihara et al. 2022).

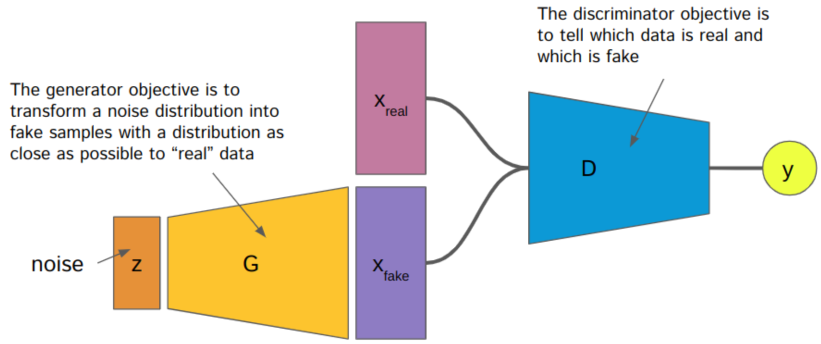

Figure 1. Overview of a Generative Adversarial Network.

2. Method

GANs are a type of generative neural network where the generative model is pitted against an adversary: a discriminative model that learns to determine whether a sample is from the model distribution or the data distribution. Competition between the generator and the discriminator leads to the generation of extremely high quality fake samples that are virtually indistinguishable from real data, this is achieved with relative simple models and moderate data quantity.

A simple schematic diagram of a GAN model is shown in Fig. 1. Several variations of GAN model exists, in this work we focus on StyleGAN2 (Karras et al. 2019), a well understood model which improves upon the basic GAN architecture in several ways, achieving remarkable generation quality and training stability.

One disadvantage of GANs over other generative models, such as autoencoders, is the lack of an easily accessible latent space representation where the images are robustly encoded. It is in those embedded representations that the complex image information is categorized and organized during training, and that could be exploited to gain insights about the original datasets. Therefore, we propose to use a technique called GAN inversion (Xia et al. 2021) which aims to invert a given image back into the latent space of a pretrained GAN model so that the image can be faithfully reconstructed by the generator from the inverted code.

In particular, we trained an additional encoder type neural network, which learns to map images to a latent vector space, such that the pretrained StyleGAN2 generator is able to reproduce the original image from the latent vector. During this training, the StyleGAN2 generator remains frozen. A simple schematic of the procedures is shown in Fig. 2.

We trained the StyleGan2 method using 314000 galaxies from HSC-SSP in the $[0.3 - 1]$ redshift range.

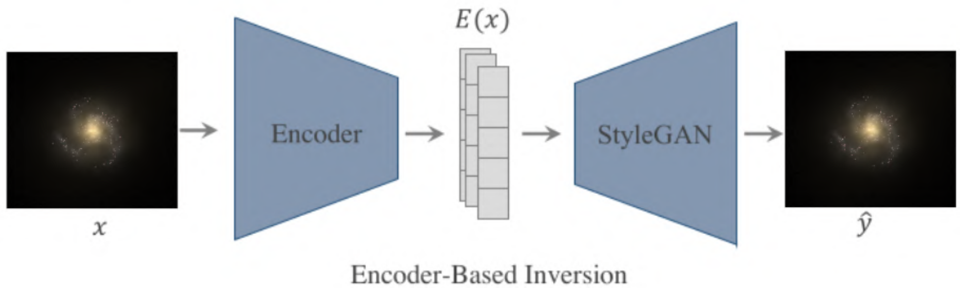

Figure 2. Overview of an encoder-based GAN inversion method.

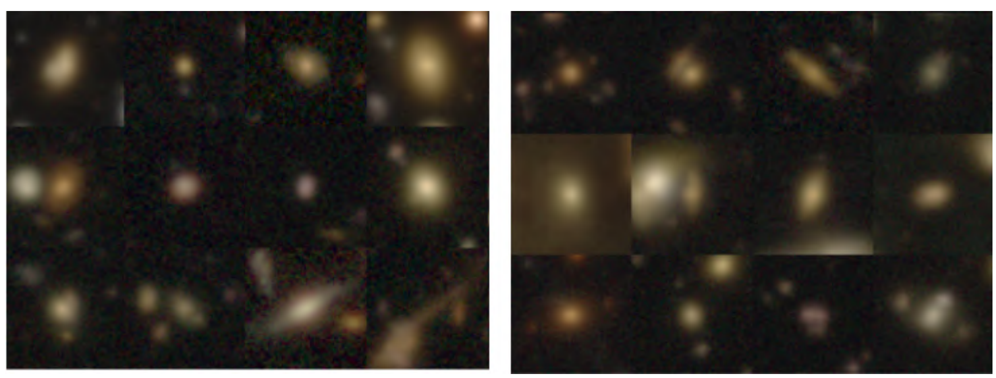

Figure 3. Examples of training HSC galaxies (left) and fake galaxies generated by StyleGAN2 (right).

3. Results

Fig. 3 compares training and generated examples from the HSC-SSP model. As can be seen, the two sets are very similar. The generated examples reproduce well the morphologies, colour, background, noise level and other subtle aspects of the original images. Occasionally, geometric artifacts are found in the generated samples, which is not uncommon in this kind of models. The generated quality can be measured by the Fréchet Inception Distance (FID, Heusel et al. 2017) score, which is 2.05 in this case, an excellent value, consistent with the general perception of good quality.

Fig. 4 shows an example of GAN inversion result. The image on the left shows a galaxy that was not used during the StyleGAN2 training, the image on the right shows the generated image from the encoded representation. As can be appreciated, the reconstructed image recovers the most important features and shows a good resemblance with the original image. This indicates that we were able to successfully generate a well-behaved latent space which has the potential to give us further insights into galaxy morphologies.

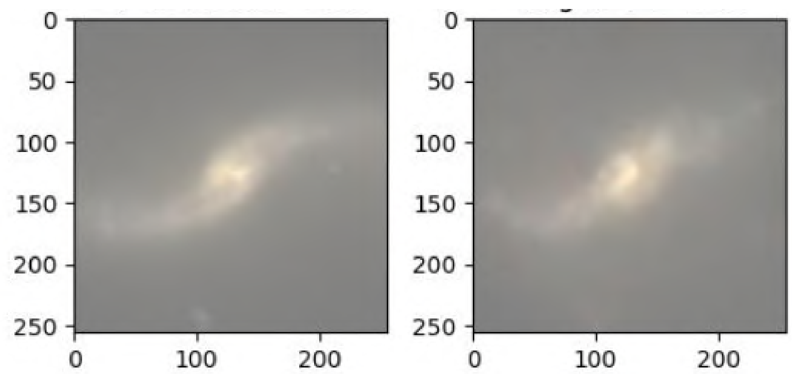

Figure 4. Examples of an original galaxy image (left) and its reconstruction generated from our enconder-based GAN inversion method (right).

4. Conclusions

In this work, we presented the initial components of an unsupervised galaxy morphology classification method based on generative neural networks. We showed that our method successfully achieves the two fundamental tasks for such a system: 1) the capacity to learn to generate good quality galaxy images and 2) the capacity to encode previously unseen galaxy images into the latent space of the neural network.

References

Aihara H., et al. 2022, PASJ, 74, 247
Goodfellow I.J., et al. 2014, arXiv:1406.2661
Heusel M., et al. 2017, arXiv:1706.08500
Karras T., et al. 2019, arXiv:1912.04958
Kingma D.P., Welling M. 2019, arXiv:1906.02691
Lotz J.M., Primack J., Madau P. 2004, AJ, 128, 163
Sohl-Dickstein J., et al. 2015, arXiv:1503.03585
Xia W., et al. 2021, arXiv:2101.05278

Asociación Argentina de Astronomía
Massive Stars and Interacting Binaries: 1st Padova–Buenos Aires Workshop
AAA Workshop Series 14, 2026
L.J. Pellizza, G.J. Escobar, S.E. Pedrosa & S.E. Nuza, eds.

Cosmic rays from massive star binaries as crucial agents for the reionization of the Universe

L. Carvalho[1], L.J. Pellizza[1], G.J. Escobar[2]

[1] *Instituto de Astronomía y Física del Espacio (IAFE), Argentina*
[2] *Università degli studi di Padova, Italia*

Abstract. We study how high-energy cosmic ray electrons from massive binaries drive IGM reionization via Inverse Compton-triggered secondary photoionization. These leptonic cascades produce up to 10^6 ionizations per primary electron within 10 Mpc, acting as essential long-range agents that complement stellar UV photons during the epoch of reionization.

1. Introduction

Massive binaries are efficient laboratories for non-thermal particle acceleration in the early universe. Through the collision of powerful stellar winds, kinetic energy is converted into high-energy cosmic rays (CRs) (Pittard et al. 2021). High-mass X-ray binaries and their transition into microquasars with relativistic jets also accelerate particles to relativistic energies (Mirabel 2011; Bosch-Ramon & Khangulyan 2009; Escobar et al. 2021,2022). Furthermore, supernova remnants provide the main sources of particle acceleration on galactic scales (Bell 2013). Consequently, massive binaries are a primary source of feedback between galaxies and the intergalactic medium (IGM), providing ionizing radiation and CRs.

The thermodynamic evolution of the IGM was fundamentally altered by the first stellar populations around redshift $z \sim 20$ (Peacock 1999). Their interaction with neutral hydrogen and helium triggered a global phase transition, driving a rise in the ionization fraction. This Epoch of Reionization (EoR) is constrained by E-XQR-30 quasar samples to have concluded by $z \sim 5.3$ (Davies et al. 2024).

While UV emission from early stars is the primary candidate for driving reionization (Robertson et al. 2010), its efficacy depends on the escape fraction ($f_{\rm esc}$) of ionizing photons. Recent JWST observations suggest that while $f_{\rm esc}$ might be higher in low-mass galaxies than previously assumed (Topping et al. 2024), the ability of these photons to ionize the deep IGM is still debated (Ferrara et al. 2013; Izotov et al. 2016).

A compelling alternative lies in CRs leaking from early galaxies. These particles, accelerated in wind collisions, microquasar jets, or primordial supernova shocks, transport substantial energy across cosmological distances (Heinz & Sunyaev 2002; Sotomayor et al. 2019; Douna et al. 2018). As they propagate, CRs interact with matter, radiation, and magnetic fields, depositing kinetic energy that facilitates reionization and pre-heating.

Building on foundational works (Tueros et al. 2014; Leite et al. 2017; Douna et al. 2018), this study extends the electron energy spectrum and spatial range using a refined numerical approach. We focus on the energy transfer between the leptonic CR component and the IGM, considering the dominant interaction during the EoR (Carvalho et al. 2024). Using Monte Carlo simulations, we model energy injection via electromagnetic cascades (EMC) to assess the role of CRs.

2. Method

Modeling EMCs in the primordial IGM requires accounting for the non-linear coupling between particle populations. Due to the stochastic nature of these interactions and the wide energy scales involved, the system is analytically unapproachable. We utilize an upgraded version of the Monte Carlo code UTOPIA (Pellizza et al. 2010; Douna et al. 2018). Simulations consider a spherical volume of $R = 10$ Mpc centered on a point-like source. Within this volume, we model a neutral hydrogen density of $n_{\rm HI} = 250.2\ {\rm m}^{-3}$ (Sazonov & Sunyaev 2015), a free electron field characterized by a residual ionization fraction $x_e \approx 2 \times 10^{-4}$, and a target photon field following the Planck Collaboration (2020) parameters. The model incorporates cooling and interaction processes—collisional ionization, Inverse Compton (IC) scattering, Coulomb elastic scattering, and photoionization—identified as dominant drivers of IGM evolution.

Building upon Carvalho et al. (2024), we implemented two optimizations to UTOPIA. First, we introduced a hybrid treatment for Compton scattering based on a dynamic energy threshold. Interactions where the secondary photon energy is lower than a predetermined value are now modeled via a continuous energy loss approximation rather than through individual stochastic sampling. Second, we integrated lookup tables for total cross-sections. These features reduced computational time by an order of magnitude, allowing for high-precision modeling across larger volumes and higher energies.

3. Preliminary Results

Fig. 1 shows the cumulative number of ionization events per number of incident particle ($N_{\rm ion}/N_{\rm inc}$) vs. distance R for electron kinetic energies $K_{\rm e}$ from 100 eV to 10 GeV. Two distinct regimes exist: for $K_{\rm e} < 1$ MeV (left panel), ionizations saturate within 10 Mpc as the energy drops below the hydrogen ionization threshold, $I_{\rm HI}$. Conversely, for $K_{\rm e} \geq 1$ MeV (right panel), EMCs propagate beyond 10 Mpc. In this regime, $N_{\rm ion}/N_{\rm inc}$ grows with $K_{\rm e}$ because secondary photons from IC scattering against the cosmic microwave background (CMB) can exceed $I_{\rm HI}$. This enhances the efficiency of CR electrons, which produce up to 10^6 ionizations per primary particle, while photon-initiated EMCs struggle to produce only a dozen ionizations under the same conditions (Fig. 2). For $K_{\rm e} \gtrsim 1$ GeV, the $N_{\rm ion}/N_{\rm inc}$ slowly decreases as the secondary cascades are produced increasingly closer to the simulation boundary, leading to increased energy leakage.

Fig. 3 illustrates the total $N_{\rm ion}/N_{\rm inc}$ relative to $K_{\rm e}$ for different physical models. Below 100 keV, the results for purely collisional models ($N_{\rm ion}$) and those including IC scattering grow linearly and nearly coincide with the uppermost limit where all energy is converted into ionizations, $N_{\rm ion}^{\rm Max}$. Near $K_{\rm e} \sim 1$ MeV, a significant fraction of energy escapes the 10 Mpc volume, causing a drop that deviates from linearity. However, when photoionization is included ($N_{\rm ion}$ IC+Photoion),

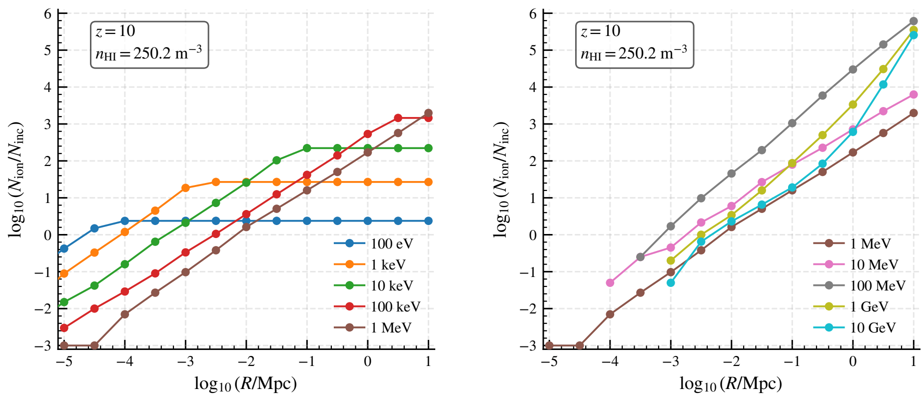

(a) $K_e \leq 1$ MeV (b) $K_e \geq 1$ MeV

Figure 1. Cumulative number of ionization events ($N_{\rm ion}/N_{\rm inc}$) vs. distance (R). Left and right panels show the low and high initial kinetic energy regimes, respectively.

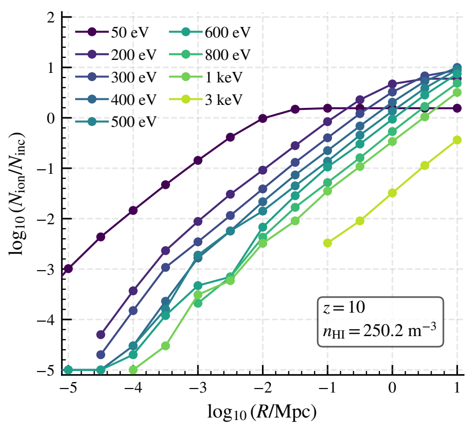

Figure 2. Cumulative number of ionization events ($N_{\rm ion}/N_{\rm inc}$) vs. distance (R) for photon initiated cascades.

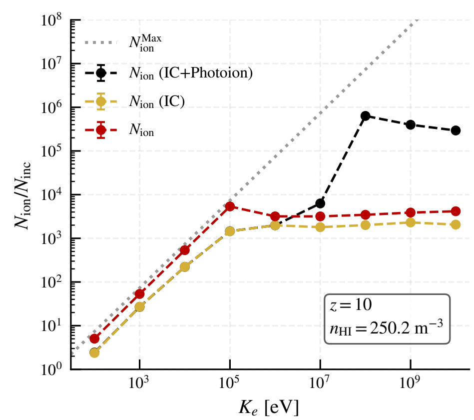

Figure 3. Ionization events ($N_{\rm ion}/N_{\rm inc}$) vs. primary electron kinetic energy ($K_{\rm e}$) for electron initiated cascades.

a sharp increase is observed beyond $K_{\rm e} \gtrsim 10$ MeV. This happens because, for sufficiently large kinetic energies ($K_{\rm e} \gtrsim 5.11$ MeV, for CMB photons at $z = 10$), it is possible for the secondary photons produced by Compton scattering against the CMB to reach energies greater than $I_{\rm HI}$. This indicates that secondary photoionization effectively re-inserts energy into the IGM that would otherwise escape beyond the established region. For $K_{\rm e} \gtrsim 1$ GeV, $N_{\rm ion}/N_{\rm inc}$ decreases because secondary cascades originate closer to the 10 Mpc boundary and because secondary photons become more energetic, which hinders the photoionization cross-section as it scales as $E_{\rm ph}^{-3}$.

4. Conclusions

We have shown that, in the context of early galaxy formation, even a relatively small population of high-energy CRs leaked from galaxies could have a disproportionate impact on the ionization state of the IGM. Unlike UV photons, which are easily absorbed in the vicinity of their sources, the IC-produced secondary photons can propagate into the neutral IGM, potentially explaining the heating and ionization requirements that UV-only models struggle to meet.

Our simulations suggest that as reionization progressed and the IGM density evolved, the "leakage" of high-energy cascades would have contributed to a global, diffuse ionizing background. This implies that CR electrons, particularly those originating from the intense lifecycle of massive binary systems, are essential components for a precise model of the EoR, acting as long-range agents that complement the localized effects of stellar UV radiation (e.g., Atek et al. 2026).

References

Atek, H. 2026, arXiv:2604.23823
Bell, A.R. 2013, Astropart. Phys., 43, 56
Bosch-Ramon, V., Khangulyan, D. 2009, IJMPD, 18, 347
Carvalho, L., Pellizza, L.J., Escobar, G.J., 2024, BAAA, 65, 240
Davies, F.B., et al. 2024, ApJ, 965, 134
Douna, V.M., et al. 2018, MNRAS, 474, 3488
Escobar, G.J., Pellizza, L.J., Romero, G.E. 2021, A&A, 650, A136
Escobar, G.J., Pellizza, L.J., Romero, G.E. 2022, A&A, 665, A145
Ferrara, A., Loeb, A. 2013, MNRAS, 431, 2826
Heinz, S., Sunyaev, R. 2002, A&A, 390, 751
Izotov, Y.I., et al. 2016, Nature, 529, 178
Leite, N., et al. 2017, MNRAS, 469, 416
Mirabel, I.F., et al. 2011, A&A, 528, A149
Peacock, J.A. 1999, Cosmological Physics, Cambridge Univ. Press
Pellizza, L.J., Orellana, M., Romero, G.E. 2010, IJMPD, 19, 671
Pittard, J.M., Vila, G.S., Romero, G.E. 2021, MNRAS, 501, 1360
Robertson, B.E., et al. 2010, Nature, 468, 49
Sazonov, S., Sunyaev, R. 2015, MNRAS, 454, 3464
Sotomayor Checa, P., Romero, G.E. 2019, A&A, 629, A76
Topping, M.W., et al. 2024, MNRAS, 529, 4087
Tueros, M., del Valle, M.V., Romero, G.E. 2014, A&A, 570, L3

Asociación Argentina de Astronomía
Massive Stars and Interacting Binaries: 1st Padova–Buenos Aires Workshop
AAA Workshop Series 14, 2026
L.J. Pellizza, G.J. Escobar, S.E. Pedrosa & S.E. Nuza, eds.

Galaxy sizes in the early Universe

P. Cataldi[1], S. Pedrosa[1], L.J. Pellizza[1], D. Ceverino[2,3], L.A. Bignone[1]

[1]*Instituto de Astronomía y Física del Espacio (IAFE), Argentina*
[2]*Dpto. de Física Teórica, Universidad Autónoma de Madrid, España*
[3]*CIAFF, Fac. de Ciencias, Univ. Autónoma de Madrid, España*

Abstract. We present preliminary results of a study of galaxy sizes at redshift $z \gtrsim 5$ using the high-resolution, zoom-in FirstLight simulations. We obtain a redshift-independent, chevron-shaped stellar mass–size relation with a peak at $M^\star \approx 10^{8.5}$ M$_\odot$. This relation is shaped by the individual evolution of galaxies, which undergo a phase of contraction at this mass scale triggered by a strong central starburst.

1. Introduction

Sizes are fundamental proxies for tracing galaxy formation history and evolutionary processes, some of which (chemical evolution, energy feedback) are driven by massive stars (Hopkins et al. 2023, and references therein). Recent JWST observations have found compact (effective radii of the order of a few hundred parsecs), red, massive (stellar masses $M^\star \gtrsim 10^{10}$ M$_\odot$) galaxies at redshifts $z > 7$. These also show high star formation rate densities and evidence of inside-out growth (e.g. Morishita et al. 2024). Their origin is still under debate, as it is the nature of the stellar mass–size relation at high z. Some authors claim that this relation is inverted (e.g. Baggen et al. 2023), whereas others argue that it remains normal (e.g. Morishita et al. 2024). This highlights some open questions on the mechanisms driving galaxy formation in the early Universe.

Several simulations with varying baryonic physics and resolution (Ni et al. 2020; Lovell et al. 2021; Kannan et al. 2022) reveal an intrinsic mass–size relation with a hump around $M^\star \sim 10^8$–10^9 M$\odot$. A characteristic *turn-on* mass marks the transition from low-mass galaxies, in which feedback-driven outflows dominate and sizes grow, to massive systems shaped by disk instabilities, angular momentum loss, and subsequent compaction (Lapiner et al. 2024). However, other simulations (Shen et al. 2024) find no compaction phase for low-mass galaxies ($M^\star \sim 10^{7-9}$ M$_\odot$) at $z > 3$. These rather exhibit rapid size fluctuations driven by the interplay between feedback outflows and cold inflows. This preserves the overall size–mass relation, increasing its scatter rather than reversing its slope.

Thus, whether a true hump or inversion exists remains under debate. Given the conflicting results from both observations and simulations regarding the high-redshift size–mass relation, a comprehensive investigation is required to clarify the issue and underpin the underlying physical processes. A step forward can be made by using zoom-in simulations, especially devised to explore galaxy evolution at Cosmic Dawn, such as the FirstLight suite (Ceverino et al. 2017). Their high resolution allows to precisely trace the mass–size relation through a large

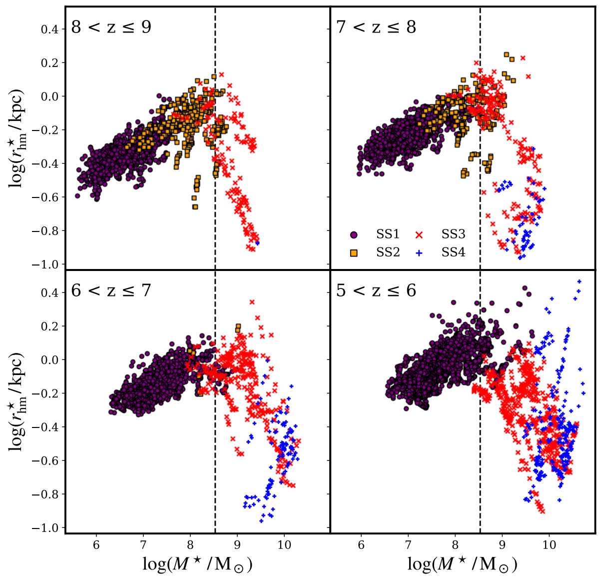

Figure 1. Stellar mass–size relation across redshift as a result of evolutionary stages: expanding galaxies (purple dots) lie in the ascending branch, at the top of which we find objects showing the onset of contraction (orange squares). The descending branch is populated by contracting galaxies (red crosses), whereas at its bottom, the systems show an incipient re-expansion (blue plus symbols). The dashed vertical line marks the *turn-on* stellar mass, $M^{\star}_{\rm on} = 10^{8.5}$ M$_{\odot}$.

range of masses. Here we present some preliminary results of such a study; the full investigation can be found in Cataldi et al. (2025).

2. Simulations and results

We use a subsample from the FirstLight cosmological zoom-in simulations, which achieve ~ 10 pc spatial resolution and include both thermal and radiative feedback (for details see Ceverino et al. 2017). The sample comprises 169 galaxies with stellar masses spanning from $\sim 10^6$ to $10^{10.5}$ M$_{\odot}$, tracked across 45 snapshots between $z = 9$ and 5.25. It enables us to study the growth of galaxies during Cosmic Dawn, and the possible inversion of the size–mass relation.

Fig. 1 shows the relation between the stellar mass $M^{\star}$ and the galaxy size (measured by the half-mass radius $r^{\star}_{\rm hm}$) for the sample. A chevron shape is evident at all redshifts, with a tight ascending (*normal*) branch in which galaxy size increases with its mass, and a descending one with larger scatter toward lower redshifts. The peak separating both branches occurs at $M^{\star}_{\rm on} \approx 10^{8.5}$ M$_{\odot}$, which we call *turn-on* mass. The fact that the loci of both branches are roughly constant with redshift suggests that the relation follows the evolutionary path of galaxies. We confirmed this by analysing the individual mass–size evolution of each galaxy in our sample. We divided our sample into four subsamples char-

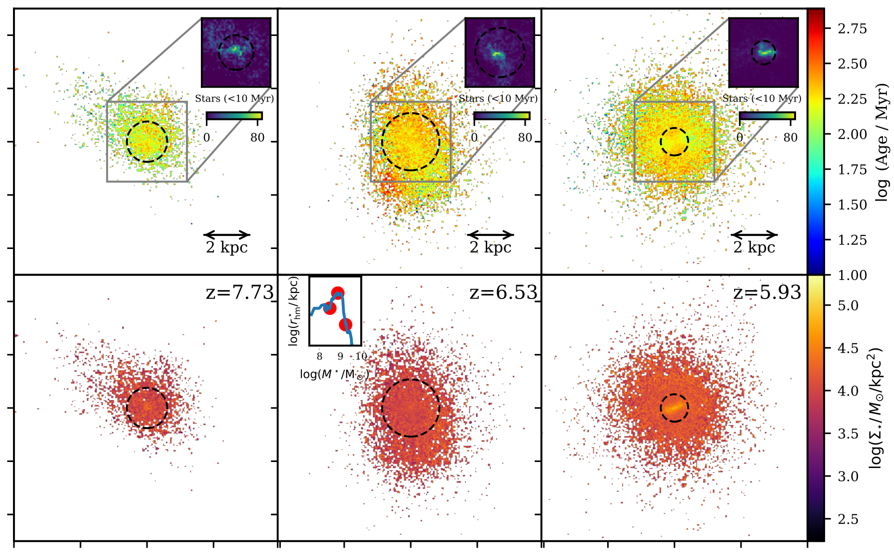

Figure 2. Edge-on view of a galaxy at its maximum size (centre panels), and ~ 100 Myr before (left panels) / after (right panels) attaining it. Colours indicate the stellar ages (top) and surface densities (bottom). The black dashed circle marks the half-mass radius $r^\star_{\rm hm}$. Inset panels highlight newly formed stars within $r^\star_{\rm hm}$ (top) and the mass–size relation, with the red dots marking the loci of the three snapshots (bottom).

acterised by distinct evolutionary patterns: (a) galaxies undergoing continuous expansion over the redshift interval studied (purple dots in Fig. 1), (b) galaxies with an initial expansion phase prior to compaction (orange squares), (c) galaxies undergoing a compaction phase (red crosses), and (d) galaxies with a re-expansion phase (blue plus symbols). We interpret these as different stages of a single evolutionary sequence in which galaxies expand, then contract, and subsequently re-expand. The existence of the characteristic mass $M^\star_{\rm on}$ suggests that stellar mass is the main driver of the compaction process. Similarly, a *turn-off* mass $M^\star_{\rm off} \approx 10^{9.6}$ M$_\odot$ appears to mark the point where galaxies start to re-expand, although the small sample of galaxies with masses above $M^\star_{\rm off}$ prevents the extraction of meaningful results on this phase. Variations in the critical masses likely reflect differences in star formation histories and environmental or merger effects.

Fig. 2 illustrates the representative case of a galaxy that undergoes rapid compaction. The sequence reveals the transition from an early, spatially extended star-forming phase characteristic of systems growing inside-out, to a compact distribution of stars concentrated at the galaxy centre. This suggests that contraction is driven by the triggering of a strong starburst in the central regions of galaxies. As the half-mass radius depends on the distribution of the stellar mass, a large mass of stars must be formed in these regions to stop and finally reverse its increase.

3. Conclusions

We identify a population of compact galaxies formed at high redshift via a mechanism that temporarily stops normal inside-out growth, rapidly shrinking their stellar distributions to sizes comparable to those observed. This process produces a chevron-shaped stellar mass–size relations with a peak mass $M^{\star}_{\rm on} \approx 10^{8.5}\,{\rm M}_{\odot}$, independent of redshift, indicating that stellar mass is its main driver. Growth then resumes after this compaction, near a characteristic mass $M^{\star}_{\rm off} \simeq 10^{9.6}\,{\rm M}_{\odot}$. Our results suggest that the origin of compaction is the triggering of a strong starburst at the central regions of galaxies, which supports a wet compaction scenario (Dekel & Burkert 2014), which may be driven by inflows of cold gas from the outskirts. Future work will investigate the underlying physical mechanisms responsible for sustaining and regulating this process.

Acknowledgements. Authors acknowledge support by ANPCyT through PICT 2020-00582, and the European Union's Horizon 2020 Research and Innovation Programme (Marie Skłodowska-Curie grant agreement No 734374 / LACEGAL). DC is supported by research grants PID2021-122603NB-C21 funded by the Ministerio de Ciencia, Innovación y Universidades (MICIU/FEDER) and CNS2024-154550 funded by MICIU/AEI/10.13039/501100011033. The authors gratefully acknowledge the Gauss Center for Supercomputing for funding this project by providing computing time on the GCS Supercomputer SuperMUC at Leibniz Supercomputing Center (Project ID: pr92za), computer resources at MareNostrum, and technical support by the Barcelona Supercomputing Center (RES-AECT-2020-3-0019).

References

Baggen, J.F.W., et al. 2023, ApJ, 955, L12

Cataldi, P., et al. 2025, arXiv:2510.05299

Ceverino, D., Glover, S.C.O., Klessen, R.S. 2017, MNRAS, 470, 2791

Dekel, A., Burkert, A. 2014, MNRAS, 438, 1870

Hopkins, P.F., et al. 2023, MNRAS, 525, 2241

Kannan, R., et al. 2022, MNRAS, 511, 4005

Lapiner, S., et al. 2023, MNRAS, 522, 4515

Lovell, C.C., et al. 2021, MNRAS, 500, 2127

Morishita, T., et al. 2024, ApJ, 963, 9

Ni, Y., et al. 2020, MNRAS, 495, 2135

Shen, X., et al. 2024, arXiv:2402.08717

Asociación Argentina de Astronomía
Massive Stars and Interacting Binaries: 1st *Padova–Buenos Aires Workshop*
AAA Workshop Series 14, 2026
L.J. Pellizza, G.J. Escobar, S.E. Pedrosa & S.E. Nuza, eds.

Constructing a mass transfer stability criterion for population synthesis studies. I. Angular momentum loss via Jeans mode and isotropic re-emission

M. Echeveste[1,2], G.J. Escobar[3,4]

[1] *Osservatorio Astrofisico di Arcetri - INAF, Italia*
[2] *Instituto de Astrofísica de La Plata (IALP), Argentina*
[3] *Instituto de Astrofísica de Canarias, España*
[4] *Universidad de La Laguna, Tenerife, España*

Abstract.
The stability of mass transfer through Roche-lobe overflow in binaries mainly depends on whether the donor star can remain within its Roche lobe throughout the process. In this article, we derive an expression for the response of the Roche lobe radius to mass loss in the general case where the mass transfer is non-conservative. We explore its impact on the mass transfer stability for different mass transfer efficiencies and angular momentum loss modes. We consider main sequence, subgiant, and white dwarf donors. We show that if the angular momentum is lost from the accretor, inefficient mass transfer allows binaries with larger mass ratios (donor over accretor mass) to undergo stable mass transfer. If the angular momentum is lost from the donor, stable mass transfer occurs at even larger mass ratios, with the exception of white dwarf donors, in which inefficient mass transfer leads to stable scenarios at smaller mass ratios.

1. Introduction

Mass transfer (MT) in interacting stellar binaries gives rise to a variety of interesting astrophysical objects. Despite its pivotal role in binary evolution, the MT process remains not fully understood. As a first step in any simplified analysis, it is crucial to distinguish between stable and unstable modes of MT. This is essential as these two cases shape the outcome of the interaction. On the one hand, unstable MT generally leads to the engulfment of the accretor by the donor's envelope, which can preclude a merger of the two stars. Even if the stars avoid merging, there is a large amount of matter ejected from the system, and also angular momentum is lost, leading the two stars to end up in a very close orbit. On the other hand, stable MT always leads to detached configurations. Stable MT can still lead to a fraction of the mass being lost from the system, which is usually referred to as non conservative MT.

The stability of the MT critically depends on the response of the donor star to mass loss, and on how this response competes with the response of the radius of its Roche lobe to mass loss. Tipically, in order to avoid unstable MT, the star should avoid increasingly overflowing its Roche lobe, and therefore, its radius should not increase faster (or decrease slower) than it's Roche lobe radius. The response of the star's radius can be characterized by the adiabatic index $\zeta_{\rm ad} = (d\ln R_{\rm d}/d\ln M_{\rm d})|_{\rm ad}$, where $M_{\rm d}$ and $R_{\rm d}$ are the mass and radius of the donor star. The value of this index depends on the stellar structure, in particular, on the energy transport mechanism that dominates in the envelope. Briefly, convective envelopes tend to expand as a response to mass loss, while radiative envelopes tend to shrink. The response of the Roche lobe radius, $R_{\rm L}$, is expressed by the index $\zeta_{\rm L} = d\ln R_{\rm L}/d\ln M_{\rm d}$, which depends on the variation of the mass ratio and semi-major axis of the binary. With these indices, $\zeta_{\rm L} > \zeta_{\rm ad}$ implies instability and $\zeta_{\rm L} \leq \zeta_{\rm ad}$ implies stability at the onset of a Roche lobe overflow phase. During the subsequent evolution, the stability of MT also depends on the response of the accretor, since its Roche lobe overflow drives the system into contact, which may lead to a common envelope or a direct merger.

In population-synthesis codes, the expression of $\zeta_{\rm L}$ by Tout et al. (1997) is usually applied to calculate the critical mass ratio $q_{\rm c}$, which marks the transition between stable and unstable mass transfer, defined by $\zeta_{\rm ad} = \zeta_{\rm L}$. This expression is deduced under conservative considerations, i.e. no mass nor angular momentum is lost from the binary. However, the same values of $q_{\rm c}$ derived from the conservative case are usually employed even in the non-conservative cases (e.g. BSE -Hurley et al. 2000, 2002; SEVN -Spera et al. 2015, 2019, Iorio et al. 2023). In this article, we will derive a more general expression for $\zeta_{\rm L}$ by removing the conservation assumption and discuss its implications in the stability of the MT. In Sect. 2 we describe the procedure, while in Sect. 3 we show our preliminary results. In Sect. 4 we present our conclusions.

2. Procedure

Analogously to Tout et al. (1997), we use the approximation of the Roche lobe radius given by Eggleton (1983),

$$\frac{R_{\rm L}}{a} = 0.44\frac{q^{0.33}}{(1+q)^{0.2}}, \tag{1}$$

valid for $0.1 < q < 10$. Here, $R_{\rm L}$ is the Roche lobe of the donor star, $q = M_{\rm d}/M_{\rm a}$, $M_{\rm a}$ is the mass of the accretor, and a is the semi-major axis. Assuming the binary is circularized, the orbital evolution of the system follows

$$2\frac{\dot{J}}{J} = \frac{\dot{a}}{a} + 2\frac{\dot{M}_{\rm d}}{M_{\rm d}} + 2\frac{\dot{M}_{\rm a}}{M_{\rm a}} - \frac{\dot{M}_{\rm d}+\dot{M}_{\rm a}}{M_{\rm d}+M_{\rm a}}, \tag{2}$$

where J is the angular momentum of the system.

To describe non-conservative MT, we follow the definitions given by Pols (2018) and introduce the parameters β and γ, which regulate the efficiency of the MT process, i.e the fraction of mass and angular momentum transferred.

$$\dot{M}_{\rm a} = -\beta\dot{M}_{\rm d}, \quad h_{\rm loss} = \frac{\dot{J}}{\dot{M}_{\rm d}+\dot{M}_{\rm a}} = \gamma\frac{J}{M_{\rm d}+M_{\rm a}}. \tag{3}$$

Using Eqs. (1)–(3) we deduce the expresion

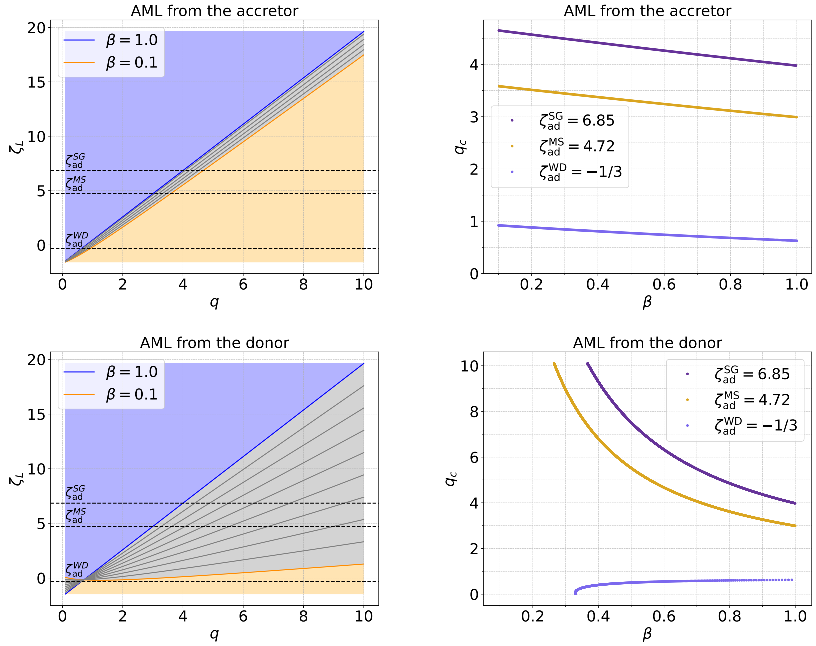

Figure 1. Left column: Roche lobe index as a function of q. The extreme cases β =1.0 and β =0.1 are shown in blue and orange while intermediate values of β appear in gray. The horizontal dashed lines are set at $-1/3$, 4.72, and 6.85, representing the value of $\zeta_{\rm ad}$ for WD, MS stars, and SG respectively. Right column: critical mass ratio as a function of β for different values of $\zeta_{\rm ad}$. Each row of plots corresponds to a mode of AML (upper row: case i), lower row: case ii)).

$$\zeta_{\rm L} = -1.67 + 2(1-\beta)(\gamma + 1/2)\frac{q}{q+1} + q\beta\left(2.33 - \frac{0.2(1+q\beta)}{\beta(1+q)}\right), \qquad (4)$$

which for $\beta = 1$ reduces to that of Tout et al. (1997), i.e. $\zeta_{\rm L} = -1.67 + 2.13q$.

3. Results

In this work, we analyse two modes of angular momentum loss (AML): i) If it proceeds isotropically from the vicinity of the accretor (usually referred to as isotropic re-emission), then $\gamma = q$, ii) if the mass is lost from the donor star (fast mode or Jeans mode), then $\gamma = q^{-1}$ (e.g. Willcox et al. 2023).

In Fig. 1, each row corresponds to a different mode of AML. The plots in the left column show $\zeta_{\rm L}$ as a function of q for different values of β. We recall that MT becomes dynamically unstable when $\zeta_{\rm L} > \zeta_{\rm ad}$, and stable otherwise. For instance, in the upper-left plot, we can follow the horizontal dashed line at $\zeta_{\rm ad}^{\rm SG} = 6.85$, a commonly adopted value for subgiant (SG) donors. For conservative MT ($\beta = 1$), stability is achieved for mass ratios $q < 4$. In contrast, if MT is highly non-conservative ($\beta = 0.1$), the critical mass ratio increases to $q_c \simeq 4.7$. This dependence of q_c on β is illustrated in the right column of the figure, which also includes results for two additional values of ζ_{ad} representative of main-sequence stars (MS, $\zeta_{ad}^{MS} = 4.72$) and white dwarfs (WD, $\zeta_{ad}^{WD} = -1/3$). As shown in the bottom-left panel of Fig. 1, the gray zone in the plot is larger if the angular momentum is lost from the donor. As a consequence, q_c grows faster when β decreases for MS or SG donors. Conversely, for WD donors q_c slightly decreases with β. Besides, there is a minimum value that β can take from which q_c exists. If β is low enough, it is not possible to define a q_c since MT is always stable (for MS and SG stars) or unstable (for WD).

4. Conclusions

A more general expression for ζ_L that includes non-conservative MT in its derivation has been proven to have an impact on the stability of MT. For the donor types we have considered, if the AML proceeds from the accretor, the new ζ_L allows binaries with larger values of q to undergo stable MT when $\beta \neq 1$. If the AML proceeds from the donor, stable MT can occur at even much larger values of q for MS and SG donors. On the contrary, for WD donors the value of q_c slightly decreases if the MT is non-conservative.

When applied to population synthesis studies, the new expression for ζ_L would produce more consistent results in the non-conservative MT scenario. We plan to include this new prescription in the population-synthesis code SEVN (Iorio et al. 2023) and investigate its effects on the formation of certain populations like blue stragglers and gravitational-wave progenitors. The results will be discussed in a forthcoming article.

Acknowledgements. Co-funded by the European Union (ERC-2022-AdG, *"StarDance: the non-canonical evolution of stars in clusters"*, Grant Agreement 101093572, PI: E. Pancino). Views and opinions expressed are however those of the author(s) only and do not necessarily reflect those of the European Union or the European Research Council. Neither the European Union nor the granting authority can be held responsible for them. GJE acknowledges support by the Spanish Ministry of Science via the Plan de Generación de Conocimiento through grant PID2022-143331NB-100.

References

Eggleton, P.P. 1983, ApJ 268, 368

Hurley J.R., Pols O.R., Tout C.A. 2000, MNRAS, 315, 543

Hurley J.R., Tout C.A., Pols O.R. 2002, MNRAS, 329, 897

Iorio, G., et al. 2023, MNRAS, 524, 426

Pols, O.R. 2018, Course Notes—Binary Stars, https://www.astro.ru.nl/~onnop/

Spera M., et al. 2015, MNRAS, 451, 4086

Spera M., et al. 2019, MNRAS, 485, 889

Tout C.A., et al. 1997, MNRAS, 291, 732

Willcox R., et al. 2023, ApJ, 958, 138

Asociación Argentina de Astronomía
Massive Stars and Interacting Binaries: 1st Padova–Buenos Aires Workshop
AAA Workshop Series 14, 2026
L.J. Pellizza, G.J. Escobar, S.E. Pedrosa & S.E. Nuza, eds.

Constructing a mass transfer stability criterion for population synthesis studies. II. Angular momentum loss from a circumbinary disc

G.J. Escobar[1,2], M. Echeveste[3,4]

[1] *Instituto de Astrofísica de Canarias, España*
[2] *Universidad de La Laguna, Tenerife, España*
[3] *Osservatorio Astrofisico di Arcetri - INAF, Italia*
[4] *Instituto de Astrofísica de La Plata (IALP), Argentina*

Abstract. The stability of mass transfer through Roche-lobe overflow in binary systems relies on the capacity of the donor star to remain within the proximity of its Roche lobe. While the response of the star's radius to mass loss depends on the stellar structure, how its Roche-lobe radius reacts depends on the binary's mass ratio and orbital configuration, and whether the mass transfer is conservative or not. In this article, we employ an expression for the response of the Roche lobe radius derived in a companion article for the general case where the mass transfer process is non-conservative. We analyze the effects of this expression on the mass transfer stability by considering different values for the mass transfer efficiency and a mode of angular momentum loss in which the lost mass settles in a circumbinary disc. We consider main sequence, subgiant, and white dwarf donors. We find that the new stability criterion favors stable MT when the circumbinary disc extracts angular momentum inefficiently, while efficient angular momentum removal promotes unstable MT. At intermediate efficiencies, the effect depends on the donor type.

1. Introduction

Mass transfer (MT) via Roche-lobe overflow in binary systems is the process responsible for the formation of a wide variety of astrophysical objects, as it drives multiple evolutionary pathways that can significantly alter the fate of the binary (e.g. common-envelope evolution, accretion on circumbinary discs, and contact phases). Understanding MT is therefore essential to model the evolution of interacting binaries. A common approach to investigate these processes is through population-synthesis simulations, which enables exploration of a large space of initial conditions and physical prescriptions at relatively low computational cost. In this context, prescriptions for the stability of MT are key factors in determining the binary outcome. While unstable MT typically leads to a common-envelope phase, possibly resulting in a merger or a compact binary after envelope ejection, stable MT generally produces detached systems.

The stability of MT depends on the response of the donor star to mass loss and on the way that this response compares with the variation of its Roche-lobe radius. Generally, most of the population-synthesis codes employ MT stability prescriptions built upon the conservative MT case. In a companion article by Echeveste & Escobar (2026), which is the first part of this study (hereafter, Part I), we deduced an expression for the Roche lobe response to mass loss in the general case where the MT is non-conservative. We explored its implications considering the following two modes of angular momentum loss: i) from the vicinity of the donor and ii) from the vicinity of the accretor. This article constitutes the second part of that investigation, where we analyze a third mode of angular momentum loss which involves the formation of a circumbinary disc when matter escapes from the outer Lagrange points L_2 and L_3. We briefly describe the model applied to this scenario in Sect. 2. In Sect. 3 we show our results, and discuss them in Sect. 4.

2. Scenario

From Part I we have that the Roche-lobe response to mass loss is given by

$$\zeta_{\rm L} = -1.67+2(1-\beta)(\gamma+1/2)\frac{q}{q+1}+q\beta\left[2.33-\frac{0.2(1+q\beta)}{\beta(1+q)}\right], 0.1 < q < 10 \quad (1)$$

where $q = M_{\rm d}/M_{\rm a}$, $M_{\rm d}$ and $M_{\rm a}$ are the masses of the donor and the accretor, respectively, and, as usual, β and γ are defined through (e.g. Pols et al. 2018, Willcox et al. 2023)

$$\begin{aligned} \dot{M}_{\rm a} &= -\beta\dot{M}_{\rm d}, \\ \gamma &= \frac{\dot{J}}{\dot{M}_{\rm d}+\dot{M}_{\rm a}}\left[\frac{J}{M_{\rm d}+M_{\rm a}}\right]^{-1}, \end{aligned} \quad (2)$$

where J is the angular momentum of the binary (orbital and from both stars), and $\dot{M}_{\rm d}$ and $\dot{M}_{\rm a}$ are the mass-loss rate from the donor and the accretion rate of the accretor, respectively. If the mass is lost from a circumbinary disk, we have

$$\gamma_{\rm CB} = \bar{\gamma}(q+2+1/q), \quad (3)$$

where $\bar{\gamma} \in (0,1)$ is the fraction of angular momentum removed from the binary, defined as in Iorio et al. (2023). The criterion for stability states that MT becomes dynamically unstable when $\zeta_{\rm L} > \zeta_{\rm ad}$ (where $\zeta_{\rm ad}$ is the adiabatic response of donor radius) and stable otherwise. Comparing with the other two modes explored in Part I, in which γ depends only on q, in this case the additional factor $\bar{\gamma}$ parametrizes how efficiently the circumbinary disc extracts orbital angular momentum. This efficiency depends on disc properties such as its mass, size, and viscous evolution timescale (Vos et al. 2015).

3. Results

The top panel of Fig. 1 shows the index $\zeta_{\rm L}$ (using $\gamma = \gamma_{\rm CB}$) as a function of q, for different values of β from 0.1 (dark orange line) to 1.0 (dark blue line), and each column shows a different value of $\bar{\gamma}$. The plots also show $\zeta_{\rm ad}$ (dashed lines) for sub-giants (SG), main-sequence (MS), and white-dwarf (WD) stars.

Light orange (blue) zones indicate configurations in which MT proceeds in unstable (stable) mode, since $\zeta_{\rm ad}$ is always greater (lower) than $\zeta_{\rm L}$ there, independently of the value of β. Instead, the gray zones show intermediate scenarios in which the stability of MT depends on β. This intermediate zone shrinks with increasing $\bar{\gamma}$, since the difference in $\zeta_{\rm L}$ between $\beta = 1$ and $\beta = 0.1$ goes with a term $-1.8(1 + q)\bar{\gamma}$, as can be obtained from Eq. 1. Thus, we see that the size of the instability zones changes dramatically with the fraction of the orbital angular momentum removed by the circumbinary disc, where higher fractions would favor more unstable scenarios. In turn, the stable MT zone changes slightly.

The bottom panel of Fig. 1 shows the critical mass-ratio $q_{\rm c}$ as a function of β for MS, SG, and WD donors. Here, $q_{\rm c}$ is solution of $\zeta_{\rm L} = \zeta_{\rm ad}$, i.e. it is the threshold value for MT stability, where $q > q_{\rm c}$ indicates unstable MT and $q \leq q_{\rm c}$ otherwise. For $\bar{\gamma} = 0.1$, $q_{\rm c}$ increases with decreasing β, regardless of the donor type. Conversely, if $\bar{\gamma} = 0.9$, $q_{\rm c}$ decreases with decreasing values of β for all donor types considered. Therefore, for each donor type, there is an intermediate value of $\bar{\gamma}$ at which $q_{\rm c}$ changes from an increasing to a decreasing function of β. This happens because for increasing $\bar{\gamma}$, the difference between $\zeta_{\rm L}$ at $\beta = 1$ and $\beta = 0.1$ decreases until it reverts its sign. This occurs at values of $\bar{\gamma}$ lower than 0.5 for WD donors, while higher values of $\bar{\gamma}$ are required for MS or SG donors. Moreover, for MS and SG donors, the scenario with $\bar{\gamma} = 0.1$ allows stable MT for values of q up to ~ 10 when MT is highly non-conservative. Particularly, MT would be stable for all the range $0.1 \leq q \leq 10$ if β is low enough (e.g. less than 0.2 in the case $\bar{\gamma} = 0.1$), while for $\bar{\gamma} = 0.9$ these values reduce to $0.1 \leq q \lesssim 3$. Similarly, but less markedly, the interval of q in which MT is stable reduces as $\bar{\gamma}$ increases for WD donors as well.

4. Conclusions

We studied the impact of a new β-dependent prescription for $\zeta_{\rm L}$ on the MT stability when the angular momentum is lost through the formation of a circumbinary disc. We showed that the fraction of removed orbital angular momentum has significant impact on the MT stability. Circumbinary discs that more efficiently remove orbital angular momentum yield to binaries undergoing unstable MT at lower donor-to-accretor mass ratios than less efficient cases. We have also shown that the stability criterion derived here favors stable MT relative to the standard conservative criterion when the circumbinary disc removes angular momentum inefficiently. Conversely, very efficient angular momentum extraction promotes unstable MT. At intermediate values of $\bar{\gamma}$, the outcome depends on donor type.

This research helps to better understand the role of MT efficiency in the determination of the Roche-lobe overflow stability. Particularly, it reflects the effects of the competition between the shrinkage of the orbit produced by angular momentum loss and the widening as consequence of mass loss (including winds; e.g. Temmink et al. 2026). This new model provides a useful prescription to include in population-synthesis codes, particularly to explore the importance of MT stability in the evolution of massive binaries and the formation of their products, such as X-ray binaries and gravitational-wave progenitors (e.g. Astudillo et al. 2025). We will discuss these implications in a forthcoming article, using this prescription in the population-synthesis code SEVN.

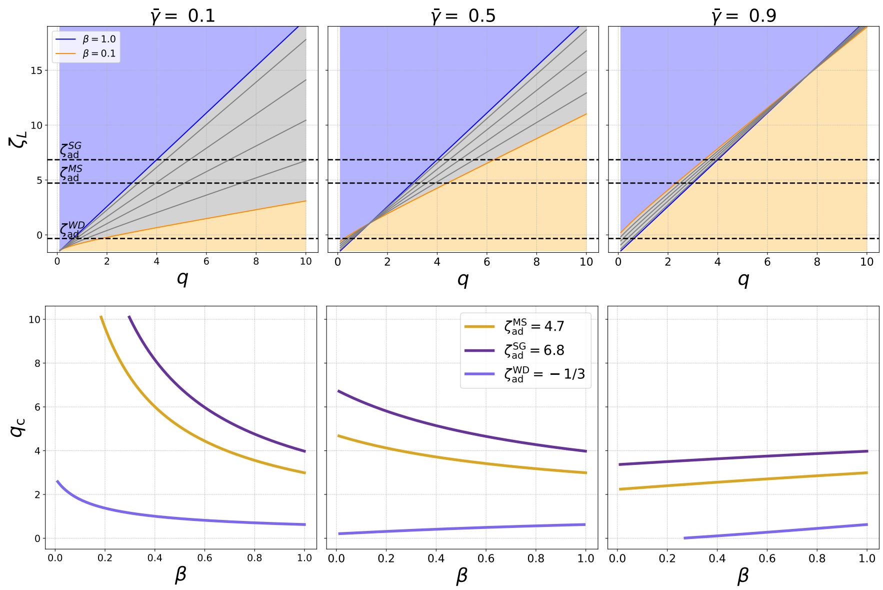

Figure 1. Top panel: $\zeta_{\rm L}$ as a function of q for different values of β from 0.1 (dark orange line) to 1.0 (dark blue line). The gray zone corresponds to intermediate values of β. Dashed lines show the adiabatic response of the donor radius for SG ($\zeta_{\rm ad}^{\rm SG} = 6.85$), MS ($\zeta_{\rm ad}^{\rm MS} = 4, 72$), and WD stars ($\zeta_{\rm ad}^{\rm WD} = -1/3$). Bottom panel: critical mass ratio, $q_{\rm c}$, as a function of β for the same three donor types shown in the top panel. Each column corresponds to a different value of $\bar{\gamma}$ (Eq. 3).

Acknowledgements. GJE acknowledges support by the Spanish Ministry of Science via the Plan de Generación de Conocimiento through grant PID2022-143331NB-100. Co-funded by the European Union (ERC-2022-AdG, *“StarDance: the non-canonical evolution of stars in clusters”*, Grant Agreement 101093572, PI: E. Pancino). Views and opinions expressed are however those of the author(s) only and do not necessarily reflect those of the European Union or the European Research Council. Neither the European Union nor the granting authority can be held responsible for them.

References

Astudillo J., et al. 2025, BAAA, 66, 361
Iorio G., et al. 2023, MNRAS, 524, 426
Pols O., et al. 1998, MNRAS, 298, 525
Temmink K.D., Justham S., Pols O.R. 2026, A&A, 709, L6
Vos J., et al. 2015, A&A, 579, A49
Willcox R., et al. 2023, ApJ, 958, 138

Asociación Argentina de Astronomía
Massive Stars and Interacting Binaries: 1st Padova–Buenos Aires Workshop
AAA Workshop Series 14, 2026
L.J. Pellizza, G.J. Escobar, S.E. Pedrosa & S.E. Nuza, eds.

An X-ray view on pulsars and their stellar environments

F.A. Fogantini[1], F. García[1], J. A. Combi[1], S. Chaty[2]

[1]*Instituto Argentino de Radioastronomía (IAR)*
[2]*Université Paris Cité, CNRS, Astroparticule et Cosmologie, France*

Abstract. We present a detailed study of the X-ray phenomenology observed in two high-mass Galactic X-ray binary systems, focusing on two neutron star supergiant systems, IGR J16320-4751 (IGR16320) and IGR J18027-2016 (IGR18027), which are heavily absorbed. Using public X-ray data from XMM-Newton and Swift/BAT, we analyse the temporal and spectral behaviour to understand the accretion patterns over different periodic timescales inherent to these systems. For the non-eclipsing binary IGR16320, modelling the orbital evolution of the X-ray absorption column and hard X-ray light curve allowed us to derive orbital parameters by assuming an isotropic radiation-driven stellar wind. In the eclipsing system IGR18027, the asymmetric absorption column and hard X-ray flux variability suggests the presence of photoionization and accretion wakes within the stellar wind, detectable over multiple orbits. These observations point to shared accretion dynamics across systems, modulated by the system's inclination, where stellar wind structures are present in both but detectable only in systems with sufficiently high inclinations.

1. Introduction

Supergiant high-mass X-ray binaries (sg/HMXBs) consist of a compact object, typically a neutron star (NS), orbiting a massive OB-type supergiant star and accreting material from its dense stellar wind. With short, circular orbits between $3-10$ days, sg/HMXBs place the NS close to the supergiant, deeply embedded in the dense stellar wind where the NS's gravity concentrates material along its orbital path, forming structures like accretion wakes (El Mellah et al. 2020). Column densities around 10^{23} cm^{-2} indicate substantial absorption as the NS passes through dense wind clumps. The NS intense X-ray emission further modulates the wind by ionizing it and forming photoionization wakes, where the wind density is shaped by the NS radiation (El Mellah et al. 2020). Additionally, line-driven instabilities in the wind create turbulent, clumpy structures, affecting mass transfer and contributing to X-ray flux variability. Systems such as IGR16320 and IGR18027, with orbital periods of 8.99 d and 4.57 d respectively, serve as potential candidates to explore wind-fed accreting systems.

2. Procedure

The XMM-Newton observatory's European Photon Imaging Camera (EPIC) includes three detectors, the pn camera (Struder et al. 2001) and the MOS cameras

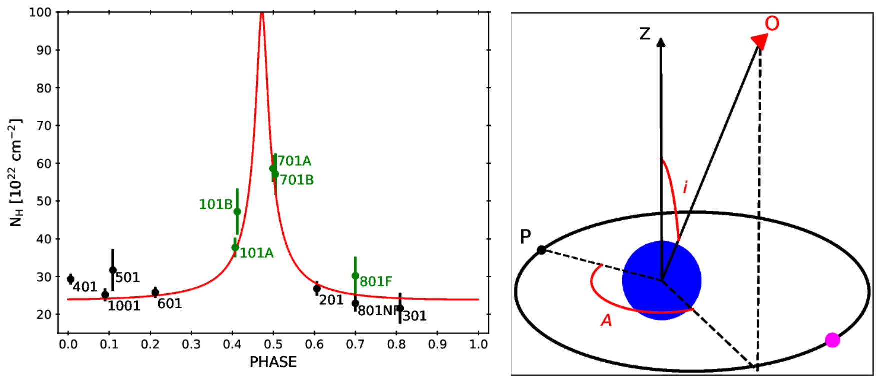

Figure 1. *Left:* Absorption column density (N_H) derived from spectral modelling as a function of the orbital phase of IGR16320. The red line corresponds to absorption from a CAK wind model. *Right:* Geometrical configuration of the orbit of the NS with eccentricity e with respect to the observer O at a position in the sky given by the inclination i and periastron argument A. Taken from García et al. (2018), A&A, 618, A61, reproduced with permission © ESO.

(Turner et al. 2001), that operate within the $0.3 - 12$ keV energy range. We reduced XMM-Newton data using the Science Analysis System (SAS) software v18.0.0. Observations of IGR16320 spanned from 2003 to 2008, while IGR18027 was observed initially in 2004 and later in 2014. High-background periods of IGR16320 were filtered using standard count rate limits, whereas for IGR J18027, an increased count rate limit of 1 c s^{-1} was applied to retain more exposure time during eclipse phases. Spectra were rebinned to have a minimum of 30 counts per bin to properly use χ^2 statistics using the SPECGROUP task from SAS. We used XSPEC (Arnaud, 1996) to model XMM-Newton spectra and to derive 90% level uncertainties. For both sources, we processed Swift/BAT $15-50$ keV lightcurves (Krimm et al. 2013), which span more than 10 years of data. Each lightcurve was folded with the best period found using the EFSEARCH task. Orbital phases were derived for the XMM-Newton observations using the ephemeris of Falanga et. al (2015).

3. Results

In the light curves of IGR16320 we observed variability over multiple timescales, including a ∼1300 s modulation consistent across energy bands, attributed to the NS rotational period (Lutovinov et al. 2005). Occasional flux increases without hardness ratio changes imply broadband flux variations rather than absorption changes. The time-averaged spectra showed a heavily absorbed continuum with an Fe edge near 7 keV, a power-law shape with a high-energy cut-off above $7 - 9$ keV, and persistent Fe Kα emission at ∼6.4 keV. Intrinsic absorption column densities ($N_{\rm H}{\sim}2 \times 10^{23}$ cm^{-2}) are in line with past studies, while higher $N_{\rm H}$ values are likely due to geometric effects. Fe-Kα flux correlated with the continuum is consistent with the Baldwin effect, where normalized Fe-Kα flux

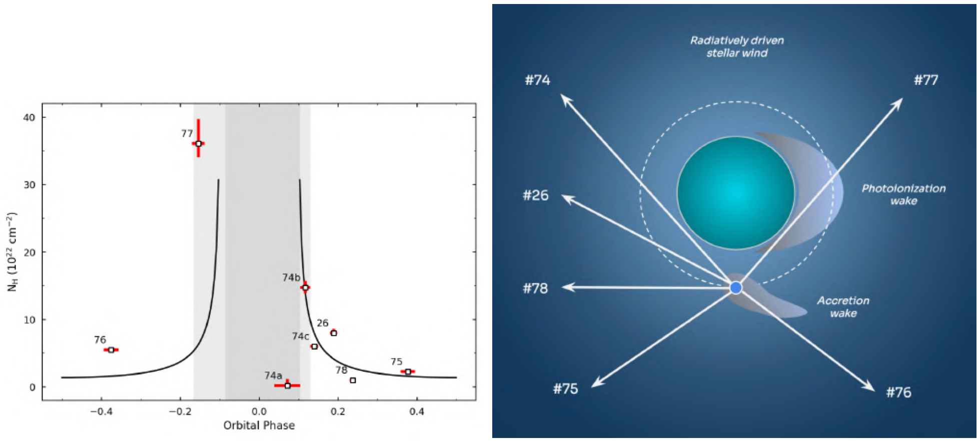

Figure 2. *Left:* Absorption column density (N_H) derived from spectral modelling as a function of the orbital phase of IGR18027. The continuos black line corresponds to absorption from a CAK wind model. The gray shaded areas correspond to the asymmetric eclipsing phases. *Right:* Stellar wind environment scenario proposed to explain the asymmetric eclipse profile seen in the data, with the photoionization wake responsible for the increased $N_{\rm H}$ in the pre-eclipse phases. Left panel taken from Fogantini et al. (2021), A&A, 647, A75, reproduced with permission © ESO.

varies with luminosity. This suggests fluorescence lines originate in a region near the NS (Chaty et al. 2008). We could successfully model the orbital modulation of the absorption column (N_H) and the high energy light curve from Swift/BAT by the application of a simple scenario involving the NS orbiting the supergiant companion that radiates a spherically symmetric wind (Castor, Abbott & Klein, 1975). The application of this model (see Fig. 1) allowed us to constrain geometrical properties of the system, such as the orbital eccentricity ($e{\sim}0.2$), the periastron argument ($A{\simeq}147$ deg) and the orbital inclination ($i{\simeq}62$ deg).

The Swift/BAT light curve of IGR18027 reveals an asymmetric eclipse profile spanning about 20% of the 4.57-day orbital period. XMM-Newton observations show similar flaring behaviour in both soft and hard X-ray bands as seen in IGR16320, consistent with stellar wind accretion. The time-averaged spectra exhibit a highly absorbed power-law continuum with Fe Kα and Fe Kβ emission lines and strong Fe absorption features.

Outside the eclipse, the absorption column is low ($\sim 10^{22}$ cm^{-2}), and only the Fe Kα line is detected. During the eclipse, the absorption column density dramatically increases ($\sim 10^{23}$ cm^{-2}), with strong Fe emission and absorption features. The correlation between the Fe Kα equivalent width and absorption column suggests that the line originates from matter close to the NS. The asymmetric eclipse profile and increased pre-eclipse absorption indicates the presence of a photoionization wake in between the NS and the donor star, as well as an accretion wake that trails the NS (see Fig. 2).

4. Conclusions

The comparison between IGR16320 and IGR18027 reveals that, despite their similar stellar components and orbital characteristics, their observed phenomenologies differ significantly due to geometric factors. The low inclination of IGR16320 places a limit on our ability to observe interactions between the NS and extended structures like the photoionization wake. This is the reason why a simpler CAK wind model is sufficient to explain the absorption column variability as well as the high-energy flux modulation for IGR16320; whereas for IGR18027 we require additional stellar wind components. Additionally, while IGR16320 shows a strong correlation between fluorescence and accretion material close to the NS, IGR18027 eclipse conditions allow for a more substantial contribution from the distant stellar wind to the observed Fe lines.

Acknowledgements. F.A.F., F.G and J.A.C. acknowledge support by PIP 0113 (CONICET). F.A.F. is postdoc fellow of CONICET. J.A.C., and F.G. are CONICET researchers. SC and FG were partly supported by the LabEx UnivEarthS, Interface project I10.

References

Arnaud K.A. 1996, ASPC, 101, 17

Castor J.I., Abbott D.C., Klein R.I. 1975, ApJ, 195, 157

Chaty S., et al. 2008, A&A, 484, 783

El Mellah I., et al. 2020, A&A, 643, A9

Falanga M., et al. 2015, A&A, 577, A130

Fogantini F.A., et al. 2021, A&A, 647, A75

García F., et al. 2018, A&A, 618, A61

Krimm H.A., et al. 2013, ApJ Suppl., 209, 14

Lutovinov A., et al. 2005, A&A, 430, 997

Strüder L., et al. 2001, A&A, 365, L18

Turner M.J.L., et al. 2001, A&A, 365, L27

Asociación Argentina de Astronomía
Massive Stars and Interacting Binaries: 1st Padova–Buenos Aires Workshop
AAA Workshop Series 14, 2026
L.J. Pellizza, G.J. Escobar, S.E. Pedrosa & S.E. Nuza, eds.

A study of early reionization sources

O. García[1,2], M. Domínguez[1,2], C. Valotto[1,2]

[1]*Fac. de Matemática, Astronomía, Física y Comp., UNC, Argentina*
[2]*Instituto de Astronomía Teórica y Experimental (IATE), Argentina*

Abstract. We used the semi-analytical code 21cmFAST (Mesinger et al. 2011) to simulate the 21-cm signal from neutral hydrogen during the Epoch of Reionization (EoR) and the Cosmic Dawn. This signal is sensitive to the evolution of the neutral hydrogen fraction and the spin temperature $T_{\rm S}$, which sets the intensity of the 21-cm emission or absorption relative to the Cosmic Microwave Background (CMB). The signal is affected by astrophysical sources that produce X-ray and ultraviolet (UV) photons, which heat and ionize the intergalactic medium (IGM). In particular, Population III and Population II stars generate ionizing photons that interact with the IGM. Binary stellar systems, especially those involving a Pop III or Pop II star accompanied by a compact object such as a black hole or a neutron star, are efficient sources of X-rays. In this work, we examine how X-rays from molecular-cooling galaxies (MCGs) influence the differential brightness temperature $\delta T_{\rm b}$.

1. Introduction

After recombination ($z \approx 1100$), neutral hydrogen (HI) became the dominant baryonic component of the intergalactic medium (IGM). The emission line of the hyperfine transition of HI at high redshift allows us to investigate the formation of the first gravitationally bound systems over large cosmological volumes. The hyperfine transition occurs when the spin of the electron changes from being parallel to antiparallel (or vice versa) with respect to the spin of the proton. In the transition from the higher energy state (triplet) to the lower energy state (singlet), a photon is emitted with a wavelength of 21 cm (frequency $\approx$ 1.42 GHz).

Multiple epochs can be identified through the HI line: the Dark Ages ($z >$ 35), before the formation of the first stars; the Cosmic Dawn ($35 > z > 15$), after the emergence of the first stars, whose UV radiation couples with the HI line through the Wouthuysen-Field effect; and the Epoch of Reionization ($z \sim 15-6$), when heating and the Wouthuysen-Field effect change the spin temperature of neutral hydrogen. That same UV radiation begins to ionize hydrogen, leading to the formation of ionized bubbles around the first mini-halos containing Pop III stars and possible mini-quasars.

There are two main approaches to detect the 21-cm emission line (Furlanetto et al. 2006): (i) its global average signal and (ii) its spatial fluctuations (HI tomography). The first approach measures the 21-cm emission over a large area, averaging out spatial fluctuations. The second one consists of detecting fluctuations using radio interferometers, which require long integration times due to the smaller amplitude of the fluctuations compared to the global signal. Current and future experiments include global-signal observations such as EDGES (Bowman et al. 2018) and interferometer experiments such as MWA (Li et al. 2019) and SKA (Koopmans et al. 2015), which will enable broader and more precise measurements of spatial fluctuations. Uncertainty remains about the role of X-ray binaries in heating the IGM and their effects on the 21-cm signal, which could potentially impact the interpretation of measurements of the Epoch of Reionization.

2. Methods

We used the 21cmFAST code (Mesinger et al. 2011) to model the intensity of the 21-cm signal in the Early Universe. The observed physical quantity is the differential brightness temperature relative to the CMB temperature T_γ, along a line of sight at the observed frequency ν, which can be expressed as (Furlanetto et al. 2006):

$$\frac{\delta T_{\rm b}(\nu)}{\rm mK} \approx 27\, x_{\rm HI}(1+\delta_{\rm nl}) \left(\frac{H}{\frac{dv_r}{dr}+H}\right)\left(1-\frac{T_\gamma}{T_{\rm S}}\right)\left(\frac{(1+z)}{10}\,\frac{\Omega_{\rm M}h^2}{0.15}\,\frac{0.023}{\Omega_{\rm b}h^2}\right)^{1/2} \quad (1)$$

where $T_{\rm S}$ is the spin temperature of the hydrogen gas (which describes the relative population of the hyperfine levels), z is the redshift, H is the Hubble constant, dv_r/dr the gradient of the proper velocity along the line of sight, h, $\Omega_{\rm b}$ and $\Omega_{\rm M}$ are the usual cosmological parameters, and $\delta_{\rm nl}(x,z) = \rho/\bar{\rho} - 1$ is the relative density fluctuation field.

The first generation of Pop III stars, which heralded the transition from the Dark Ages to the Cosmic Dawn (Furlanetto et al. 2006), were hosted in molecular-cooling galaxies (MCGs) with halo masses $M_{\rm h} < M_{\rm atom} \sim 10^{6-8}\, M_\odot$ (where $M_{\rm atom}$ is the atomic-cooling mass threshold), whereas Pop II stars formed in atomic-cooling galaxies (ACGs) with masses above $M_{\rm atom}$. Thus, Pop III stars dominate the photon budget in the Early Universe and are expected to set the timing of the cosmic-dawn 21-cm signal at $z \sim 10-20$. Later, feedback and the growth of more massive halos make MCGs subdominant, and Pop II stars are expected to drive cosmic reionization at $z \sim 5-10$.

Fig. 1 shows slices of the brightness temperature field obtained with 21cmFAST simulations in a 160 cMpc comoving box at $z = 15$ with a resolution of 1024^3 cells.

2.1. X-ray Properties of Galaxies

X-rays play a dominant role in heating the IGM during the Cosmic Dawn (Park et al. 2019). In 21cmFAST, the specific intensity of X-rays is calculated by integrating the comoving X-ray emissivity along the light cone, taking into account attenuation by hydrogen and helium in the IGM. The X-ray luminosity per unit star formation rate escaping from host galaxies is given by the ratio $L_{\rm X}/{\rm SFR}$, which follows a power-law spectrum with photon index $\alpha_{\rm X} = 1$. The luminosity in the soft band (0.5–2 keV) is calculated as:

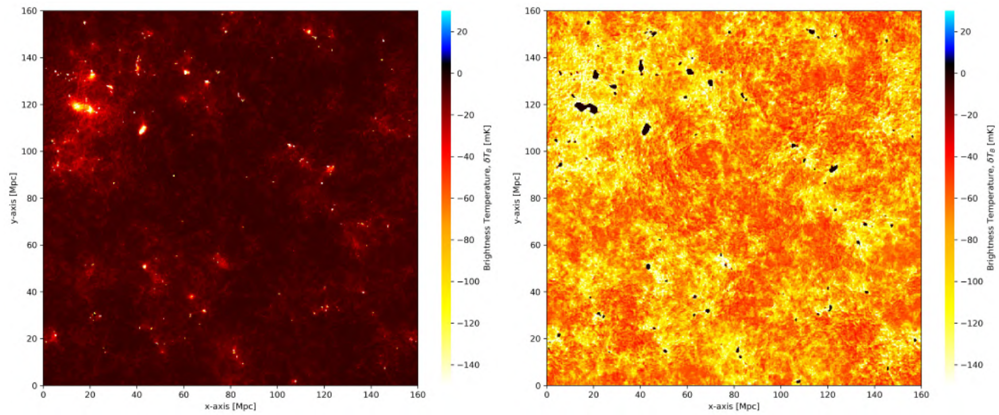

Figure 1. Brightness temperature field at $z = 15$. Effect of atomic-cooling galaxies without (left panel) and with (right panel) molecular-cooling galaxies.

$$\frac{L_X(< 2\,\mathrm{keV})}{\mathrm{SFR}} = \int_{E_0}^{2\,\mathrm{keV}} \mathrm{d}E_e \frac{L_X}{\mathrm{SFR}} \tag{2}$$

where E_0 is the energy threshold below which photons are absorbed by the host galaxy (which depends on the ISM density and metallicity).

3. Results

3.1. X-ray effect on molecular cooling galaxies (MCGs)

Molecular-cooling galaxies (MCGs) reside in mini-haloes with virial masses $M_h \sim 10^8\,M_\odot$. In these systems, the gas cools efficiently through H_2 molecules, enabling the formation of the first massive Population III (Pop III) stars. These stars evolve rapidly and produce high-mass X-ray binaries (HMXBs) that emit hard X-rays. In addition, Pop III stars emit intense ultraviolet (UV) ionizing radiation.

These astrophysical processes affect the 21-cm signal in three main ways:

(i) They modify the relative density fluctuations by forming the first massive stars inside mini-haloes.

(ii) They increase the ionization fraction of the intergalactic medium (IGM) through the emission of ionizing photons from Pop III stars.

(iii) They raise the global brightness temperature δT_b by increasing the spin temperature T_S via X-ray heating from Pop III stars and binary systems in mini-haloes.

In particular, the presence of MCGs accelerates the onset of reionization and makes the absorption trough in $\delta T_b(z)$ shallower (or even turns it into emission) compared to models that consider only atomic-cooling galaxies.

Fig. 2 shows the global differential brightness temperature $\delta T_b(z)$. The orange line corresponds to a high star-formation-rate efficiency in MCGs (which produces earlier ionization), while the black line corresponds to low efficiency (delayed ionization). Light-gray lines show high X-ray emission ($\log_{10}(L_X/\text{SFR}) = 41$), and dark-gray lines show low X-ray emission ($\log_{10}(L_X/\text{SFR}) = 38$).

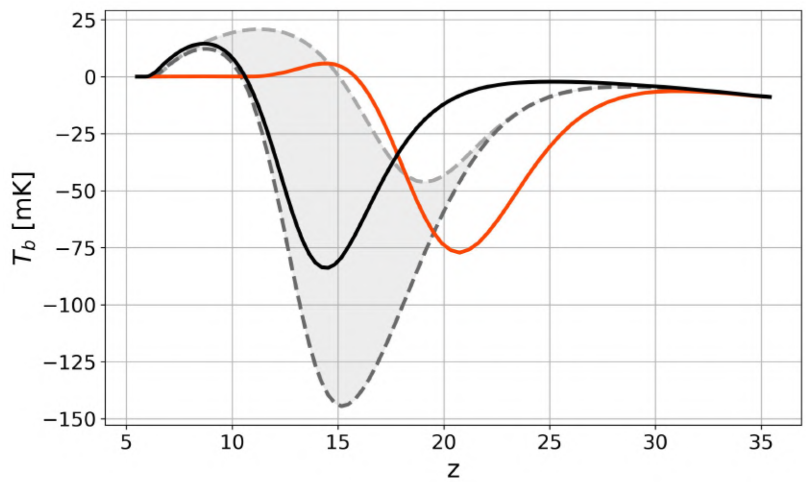

Figure 2. Global differential brightness temperature $\delta T_b(z)$ considering the effect of MCGs from $z = 35$ to the end of reionization at $z = 5$.

4. Conclusions

Our 21cmFAST simulations show that star formation in molecular-cooling galaxies has a direct impact on the 21-cm signal. High SFR efficiency in MCGs produces an earlier rise in the global brightness temperature (earlier Cosmic Dawn), while strong X-ray emission from binaries raises the spin temperature and therefore increases δT_b. These results highlight the importance of including both MCGs and X-ray sources when interpreting future 21-cm observations from the Cosmic Dawn and the Epoch of Reionization.

References

Bowman, J.D., et al. 2018, Nature, 555, 67
Furlanetto, S.R., et al. 2006, Phys. Rep., 433, 181
Koopmans, L.V.E., et al. 2015, PoS(AASKA14), 001
Li, W., et al. 2019, ApJ, 887, 141
Mesinger, A., et al. 2011, MNRAS, 411, 955
Park, J., et al. 2019, MNRAS, 484, 933

Asociación Argentina de Astronomía
Massive Stars and Interacting Binaries: 1st Padova–Buenos Aires Workshop
AAA Workshop Series 14, 2026
L.J. Pellizza, G.J. Escobar, S.E. Pedrosa & S.E. Nuza, eds.

Nebular emission from young stellar populations including binary stars

M. Lecroq[1]

[1]*Sorbonne Université, CNRS, Inst. d'Astrophysique de Paris, France*

Abstract. We investigate the nebular emission produced by young stellar populations using the new GALSEVN model. Photoionization calculations performed with the CLOUDY code confirm that accounting for binary-star processes strongly influences the predicted emission-line properties of young galaxies, in particular the strong He II $\lambda4686/\mathrm{H}\beta$ ratios commonly observed at high Hβ equivalent widths in metal-poor, actively star-forming galaxies, which have proven challenging to reproduce using previous models. Including bursty star-formation histories broadens the agreement with observations, while the most extreme He II $\lambda1640$ equivalent widths can be reproduced by models dominated by massive stars. We confirm that emission-line diagnostic criteria previously proposed to discriminate between Pop-III stars and other primordial ionizing sources in the Epoch of Reionization are suitable for very young stellar ages, and present new predictions of the ionizing-photon production efficiency of low-metallicity stellar populations.

1. Introduction

The primary ionizing sources in the Epoch of Reionization (EoR) are believed to be early stellar generations (e.g., Robertson 2022). The first massive, nearly metal-free ($10^{-11} \leq Z \leq 10^{-6}$), so-called Population III (Pop III) stars had shorter lifetimes than later stars due to their larger initial masses. This led to rapid chemical enrichment and dominance by more metal-rich ($10^{-4} \leq Z \leq 10^{-3}$) Population II (Pop II) stars, though Pop III-star formation may have continued until redshifts $z \sim 6$ (e.g., Venditti et al. 2023). Understanding the radiative properties of these early stellar populations is critical to assess their role in the reionization process.

Recent studies at various redshifts have explored the ultraviolet (UV) and optical spectra of metal-poor, star-forming, EoR-like galaxies (e.g., Stark et al. 2014, Senchyna et al. 2017, Berg et al. 2022). Observations reveal that models struggle to reproduce nebular emission from young galaxies, particularly high-energy lines such as He II recombination lines (e.g., Shirazi et al. 2012, Stanway et al. 2019, Plat et al. 2019, Olivier et al. 2022). These high-energy photons probably originate from hot, almost pure-He stars formed via binary interactions, often neglected in population synthesis models (e.g., Eldridge et al. 2012, Götberg et al. 2020). In fact, $\sim 70\%$ of massive stars in nearby populations are in binaries (e.g., Sana et al. 2012, Offner et al. 2023).

We compute the nebular emission of low-metallicity Pop II and III stellar populations by coupling the new GALSEVN model, built by combining the

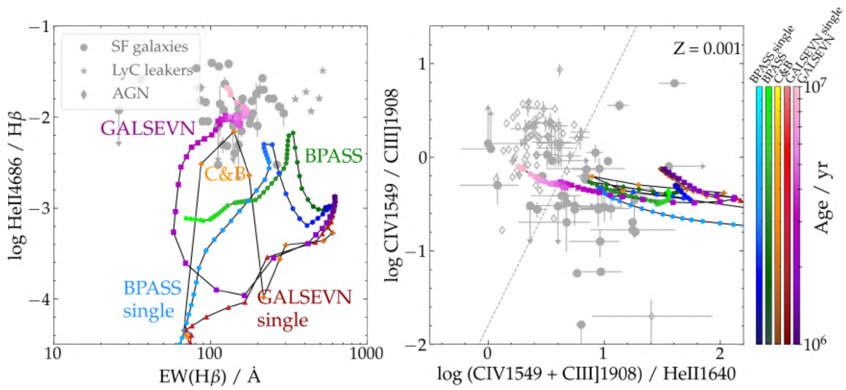

Figure 1. Optical and UV emission-line features of the reference observational sample of star-forming galaxies (filled grey symbols) and AGNs (open grey diamonds) used to calibrate the GALSEVN models. The different curves show the predictions of the GALSEVN binary- and single-star models, BPASS binary- and single-star models and C&B single-star model, colour-coded with age (see Fig. 3 of L24 for details).

SEVN (Iorio et al. 2023) binary-star population-synthesis code and the GALAXEV (Bruzual & Charlot 2003) spectral synthesis code, with the CLOUDY photoionization code (Ferland et al. 2017). We show how this model can better account for observations of UV and optical emission lines in local metal-poor star-forming galaxies —in particular strong He II emission— than previous models of both single and binary stars. We examine the location of the models in the emission-line diagnostic diagrams proposed by Nakajima & Maiolino (2022) to distinguish Pop III stellar emission from that of other potential ionizing sources in the early Universe, before investigating the production efficiency of ionizing photons, a key factor for linking the observed galaxy UV luminosity to reionization.

2. GALSEVN predictions for low-metallicity stellar populations

Following Lecroq et al. (2024; hereafter L24), we express the luminosity per unit frequency ν emitted at time t by a star-forming galaxy as

$$L_\nu(t) = \int_0^t \mathrm{d}t'\,\psi(t-t')\,S_\nu[t', Z(t-t')]\,T_\nu(t,t')\,, \qquad (1)$$

where $\psi(t-t')$ is the star formation rate at time $t-t'$, $S_\nu[t', Z(t-t')]$ the luminosity produced per unit frequency per unit mass by a single generation of stars of age t' and metallicity $Z(t-t')$, and $T_\nu(t,t')$ the transmission function of the interstellar medium (ISM). The stellar emission S_ν is computed using the code GALSEVN for populations of single and binary stars, and combined with the calculation of T_ν using the CLOUDY photoionization code (Ferland et al. 2017).

To test GALSEVN predictions for low-metallicity binary stars, we use the lowest-metallicity galaxies from the observational sample by Plat et al. (2019),

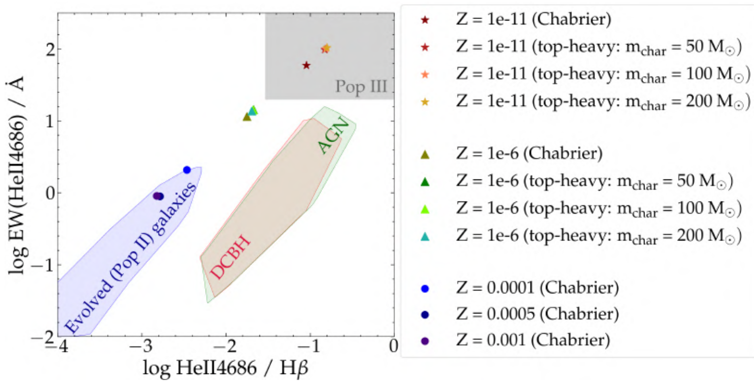

Figure 2. Diagnostic diagram from Nakajima & Maiolino (2022) distinguishing Pop III-star ionization from other high-energy sources, with GALSEVN binary-star models overlaid and regions for direct-collapse black holes (DCBHs), Pop II galaxies, and AGNs highlighted (see Lecroq et al. 2025).

supplemented with recent emission-line data (see L24). For comparison with low-redshift analogs to primeval galaxies, we use model parameters representing the average properties of this sample: interstellar metallicity, $Z_{\rm ISM} = 0.001$; H density, $n_{\rm H} = 100$ cm^{-3}; Carbon-to-oxygen abundance ratio, $C/O = 0.17$; volume-averaged ionization parameter at age $t' = 0$, $\log\langle U\rangle = -2.0$; and dust-to-metal mass ratio, $\xi_{\rm d} = 0.3$. A zero-age Chabrier (2003) initial-mass function (IMF) is adopted for primary stars in binaries, with secondary masses sampled using a Sana et al. (2012) mass-ratio distribution at age zero (as described in L24). We also model emissions from X-ray binaries and fast radiative shocks, though these have minimal impact on the relevant emission lines (L24).

Fig. 1 compares line emission predictions for single-generation stellar populations (SSPs) up to 10 Myr against the observed UV and optical line intensities and equivalent widths (EWs) for GALSEVN binary- and single-star models, alongside other recent and widely-used stellar-population models.

Fig. 1 highlights the importance of binary-star processes in modeling metal-poor, star-forming galaxies (in particular, strong He II $\lambda4686/{\rm H}\beta$ ratios) and shows good agreement between GALSEVN binary-star models and most observations, though some discrepancies remain. Variations in IMFs and more complex star-formation histories, including successive starbursts and enhanced massive-star formation, may explain extreme cases (see L24).

3. GALSEVN predictions for Population III stars

At extremely low metallicities, where no direct observations exist, the GALSEVN models may be used to compute the properties of Pop III stellar populations and provide inputs for cosmological simulations. Such predictions, based on the Pop III stellar models of Volpato et al. (2023), confirm the utility of H and He emission lines to diagnose Pop III stellar populations (Nakajima & Maiolino

2022), as shown in Fig. 2. However, distinguishing these signatures is effective only for very young stars (< 1 Myr), making observations challenging.

The production rate of H-ionizing photons ($\dot{N}$ion) and the escape fraction ($f_{\rm esc}$) of these photons into the intergalactic medium (IGM) are crucial for understanding reionization. While escaping ionizing photons are absorbed by the IGM, the ionizing photon production efficiency, $\xi_{\rm ion}^{\rm HII} = \dot{N}_{\rm ion}/L_{\rm UV}^{\rm HII}$, enables constraints on $\dot{N}_{\rm ion}$ based on the observable, non-ionizing (stellar + nebular) UV luminosity. Our modeling of the evolution of $\xi_{\rm ion}^{\rm HII}$ down to metallicities as low as $Z = 10^{-11}$ reveals high $\xi_{\rm ion}$ values, consistent with observations and sufficient for early galaxies to drive reionization, even with a low $f_{\rm esc}$ (see Lecroq et al. 2025). The natural prediction by GALSEVN of such high $\xi_{\rm ion}$ values supports the significant role of early star-forming galaxies in the reionization era.

4. Conclusions

The new GALSEVN model incorporating binary-star processes better reproduces emission-line properties of young metal-poor galaxies than previous models and offers improved diagnostics for identifying Pop III stars and constraining their potential role in reionizing the Universe.

References

Berg, D.A., et al. 2022, ApJS, 261, 31
Bruzual, G., Charlot, S. 2003, MNRAS, 344, 1000
Chabrier, G. 2003, PASP, 115, 763
Eldridge, J.J., Stanway, E.R. 2012, MNRAS, 419, 479
Ferland, G.J., et al. 2017, Rev. Mexicana Astron. Astrofis., 53, 385
Götberg, Y., et al. 2020, A&A, 634, A134
Iorio, G., et al. 2023, MNRAS, 524, 426
Lecroq, M., et al. 2024, MNRAS, 527, 9480 (L24); 2025, A&A, 695, A17
Nakajima, K., Maiolino, R. 2022, MNRAS, 513, 5134
Offner, S.S.R., et al. 2023, PASP Conf. Series, 534, 275
Olivier, G.M., et al. 2022, ApJ, 938, 16
Plat, A., et al. 2019, MNRAS, 490, 978
Robertson, B.E. 2022, ARA&A, 60, 121
Sana, H., et al. 2012, Science, 337, 444
Senchyna, P., et al. 2017, MNRAS, 472, 2608
Shirazi, M., Brinchmann J. 2012, MNRAS, 421, 1043
Stanway, E.R., Eldridge, J.J. 2019, A&A, 621, A105
Stark, D.P., et al. 2014, MNRAS, 445, 3200
Venditti, A., et al. 2023, MNRAS, 522, 3809
Volpato, G., et al. 2023, ApJ, 944, 40

Asociación Argentina de Astronomía
Massive Stars and Interacting Binaries: 1st Padova–Buenos Aires Workshop
AAA Workshop Series 14, 2026
L.J. Pellizza, G.J. Escobar, S.E. Pedrosa & S.E. Nuza, eds.

Cosmological gas accretion of Milky Way-type galaxies and the build-up of galactic discs

S.E. Nuza[1,2], C. Scannapieco[3,2]

[1] *Instituto de Astronomía y Física del Espacio (IAFE), Argentina*
[2] *Consejo Nac. de Investigaciones Científicas y Técnicas, Argentina*
[3] *Dpto. de Física, Fac. de Cs. Exactas y Naturales, UBA, Argentina*

Abstract. In this work, we present results on the assembly of stellar discs belonging to Milky Way-type galaxies in the Auriga simulated sample. We study the net accretion of gas onto the disc region as a function of time and radius to assess the feasibility of the so-called inside-out formation of galaxy discs. We found that most of the galaxies in our sample exhibit an inside-out disc growth, with younger stellar populations preferentially formed in the outer regions as accreted material turns into starts. This produces stable discs as long as late-time accretion is free from significant external perturbations.

1. Introduction

Stellar discs in spiral galaxies form as a result of cosmological gas accretion and mergers through cosmic time. In this regard, the diversity of observed galactic morphologies naturally arises from the different merger and accretion histories of each dark matter halo, leading to the formation of different components such as the galactic bulge and the thin disc. Broadly speaking, bulge formation in the Milky Way (MW) is generally believed to occur over short timescales early in the Galaxy's lifetime, whereas the disc component is thought to form over more extended periods, sustained by gas accretion at increasingly larger radii, in an "inside-out" fashion (e.g. Nuza et al. 2019).

In this contribution, we present results on the assembly of galactic discs from a sample of simulated MW-type galaxies from the Auriga project. In Sect. 2, we briefly present the simulated galaxy sample. In Sect. 3, we describe the methods used to compute the net gas accretion rate and timescales onto the stellar discs. In Sect. 4, we report our results. Finally, in Sect. 5, we present our conclusions.

2. The simulations

The Auriga sample (Grand et al. 2017) comprises a set of 30 disc galaxies similar to the MW modeled within a full cosmological context with the cosmological code AREPO (Springel et al. 2010). The cosmology adopted is consistent with the Planck collaboration XVI (2014) and the mass resolution of the model galaxies is about 3×10^5 and 5×10^4 $M_\odot$ for dark matter and gas, respectively.

The galaxy formation model includes metal-line cooling, a uniform ultraviolet background for reionization, star formation, magnetic fields, and feedback from Type II/Ia supernovae, asymptotic giant branch stars and active galactic nuclei.

The selection criteria required virial masses in the range of 1–2 $\times 10^{12}\,\mathrm{M}_\odot$ and relative isolation, with no neighboring halo with mass greater than 3% of the galaxy's mass within 9 times its virial radius. Further details on the simulated galaxies can be found in Grand et al. (2017) and Iza et al. (2022).

3. Methods

Following Iza et al. (2022), we compute the net accretion rate of gas onto the stellar disc for each simulated galaxy in the sample. The net gain/loss of gas inside a ring contained within the plane of the disc is regulated by the amount of infalling and outflowing gas particles together with the instantaneous star formation rate, responsible for gas depletion. Then, the net gas accretion rate can be written as

$$\dot{M}_{\rm net} = \frac{M_{\rm gas}(i) - M_{\rm gas}(i-1) + M_*}{t(i) - t(i-1)}, \qquad (1)$$

where $M_{\rm gas}$ is the gas mass, i and $i-1$ are indexes labelling consecutive snapshots, M_* is the stellar mass formed between them and t is the cosmic time.

Moreover, we can define a *mass-weighted time* τ to characterise the timescale of net accretion onto each ring within the stellar disc, namely

$$\tau \equiv \frac{\int_{t_{\rm i}}^{t_0} t\dot{M}_{\rm net}(t){\rm d}t}{\int_{t_{\rm i}}^{t_0} \dot{M}_{\rm net}(t){\rm d}t}, \qquad (2)$$

where $t_{\rm i}$ is a reference time from which we start the calculation and t_0 is the age of the universe. As shown in Iza et al. (2022), stellar discs in the Auriga galaxies are well defined only after the first $\sim 4\,$Gyr of evolution, hence, we adopt $t_{\rm i} = 4\,$Gyr (see also Iza et al. 2024).

4. Results

The left panel of Fig. 1 shows the net accretion rate of the Auriga galaxies as a function of cosmic time radially integrated onto the galaxy discs as defined in Iza et al. (2022). Despite differences between individual formation histories, the average net accretion rate shows a rapid increase at early times, reaching a maximum at $t \sim 6\,$Gyr, to later display an exponential-like decline until the present epoch. The vast majority of galaxies show a moderate accretion during the last $\sim 8\,$Gyr, giving rise to the formation of stable stellar discs.

The characteristic timescale of accretion as a function of normalised radius of the galaxies, integrated over their entire lifetime, can be seen in the right panel of Fig. 1. As in the previous plot, the disc radius $R_{\rm d}$ for each individual galaxy is estimated following the calculations of Iza et al. (2022). In general, typical net accretion timescales increase with radius, implying a delayed accretion of material towards the external regions of the stellar discs. This behaviour is

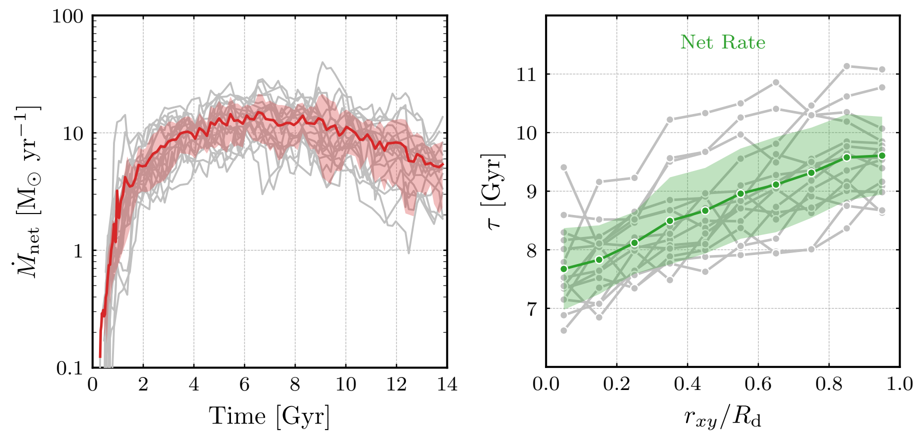

Figure 1. *Left panel:* Net accretion rate of gas integrated onto the stellar discs as a function of cosmic time. *Right panel:* Net accretion timescale of gas integrated over time as a function of normalised disc radius. In both panels, grey solid lines correspond to individual galaxies in the Auriga sample. The mean and standard deviation in each case are also shown in colour. Adapted from Iza et al. (2022, 2024).

consistent with an inside-out formation of the discs, where older stars tend to be located in the inner galaxy regions, in contrast to younger stellar populations.

It is worth noting that the Auriga sample consists of a collection of relatively isolated MW-type galaxies drawn from a large cosmological volume. However, it is known that the MW galaxy is part of the Local Group (LG), a collection of galaxies dominated by the MW and Andromeda (M31), inhabiting an environment that may affect the evolution of the individual progenitors (e.g. Nuza et al. 2014; Creasey et al. 2015; Biaus et al. 2022). Preliminary results shown in Fig. 2 suggest that MW and M31 galaxies in one of the HESTIA (Libeskind et al. 2020) LG simulations display larger net accretion rates than the overall Auriga sample. Further analyses on this matter will be performed in a future work.

5. Conclusions

In this work, we analysed a sample of simulated MW-type systems from the Auriga galaxy sample (Grand et al. 2017) to study the impact of gas accretion on the build-up of stellar discs as a function of cosmic time and radius. After computing the net accretion rate evolution of the sample and the radial dependence of the typical net accretion timescales in the simulated discs, we showed that model MW-type galaxies display a mean exponential-like behaviour with moderate rates required to build stable stellar discs during a significant fraction of the galaxy lifetimes. Additionally, preliminary results on a possible environmental dependence of gas accretion rates onto the MW-type systems were presented.

We also showed that the vast majority of galaxies in the sample display net gas accretion timescales that increase with disc radius suggesting that young

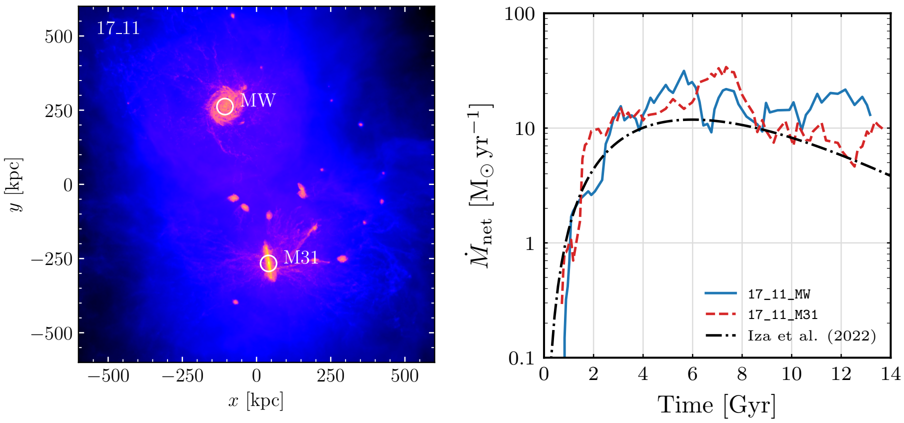

Figure 2. *Left panel:* Gas distribution in the 17_11 HESTIA realisation of the LG showing the MW and M31 galaxy candidates and their satellites. Solid circles indicate the virial radius. Adapted from Biaus et al. (2022). *Right panel:* Idem Fig. 1 (left panel) for MW and M31 candidates in HESTIA compared to the best-fit curve of MW-like galaxies in Auriga given by Iza et al. (2022).

stellar populations preferentially form in the external disc regions. These results, taken together, favour the inside-out formation scenario of stellar discs (e.g. Nuza et al. 2019; Iza et al. 2022, 2024).

Acknowledgements. We would like to thank F.G. Iza and L. Biaus for adapting the figures presented in this contribution. S.E.N. and C.S. are members of the Carrera del Investigador Científico of CONICET.

References

Biaus, L., et al. 2022, MNRAS, 517, 6170
Creasey, P., et al. 2015, ApJ, 800, L4
Grand, R.J.J., et al. 2017, MNRAS, 467, 179
Iza, F.G., et al. 2022, MNRAS, 517, 832
Iza, F.G., et al. 2024, MNRAS, 528, 1737
Libeskind, N.I., et al. 2020, MNRAS, 498, 2968
Nuza, S.E., et al. 2014, MNRAS, 441, 2593
Nuza, S.E., et al. 2019 MNRAS, 482, 3089
Planck collaboration XVI 2014, A&A, 566, A54
Springel, V. 2010, MNRAS, 401, 791

Asociación Argentina de Astronomía
Massive Stars and Interacting Binaries: 1st Padova–Buenos Aires Workshop
AAA Workshop Series 14, 2026
L.J. Pellizza, G.J. Escobar, S.E. Pedrosa & S.E. Nuza, eds.

High-mass X-ray binary hosts in the local Universe

L.J. Pellizza[1], M.B. Badaracco[1], N.E. Chisari[2], G.J. Escobar[3], S.E. Pedrosa[1], L.A. Bignone[1]

[1]*Instituto de Astronomía y Física del Espacio (IAFE), Argentina*
[2]*Utrecht University, The Netherlands*
[3]*Instituto de Astrofísica de Canarias, España*

Abstract. A precise knowledge of the luminosities of local high-mass X-ray binary populations is crucial to assess their dependence on the host galaxy metallicities, and therefore the contribution of these systems to the energy feedback in the early Universe. In this work we use galaxy formation simulations to investigate the ability of recently published models for the X-ray luminosity of these populations to describe the properties of the observed host galaxies. We find that unsteady disk models that take into account the detectability of the sources give a fairly good agreement with observations.

1. Introduction

High-mass X-ray binaries (HMXBs) are evolved systems comprising either a neutron star or black hole orbiting a high-mass ($\gtrsim 8\,\mathrm{M}_\odot$), non-collapsed companion. The compact object accretes matter from the star, which creates an X-ray emitting disk around the former (Fabbiano 2006, and references therein). Part of the infalling matter is ejected by winds blowing from the disk and relativistic jets launched from its innermost regions (e.g., Mirabel et al. 1992), injecting energy into the ambient medium (Feng & Soria 2011) and producing cosmic rays (Heinz & Sunyaev 2002; Escobar et al. 2021; Escobar et al. 2022).

The large energy feedback of HMXBs may play an important role in the modification of their environment. Some authors claim that they have contributed to the regulation of the cosmic star formation in the early Universe, and to the heating and reionization of the intergalactic medium at Cosmic Dawn (e.g., Mirabel et al. 2011, Fragos et al. 2013, Artale et al. 2015, Douna et al. 2018). However, the importance of HMXBs as feedback sources is still a matter of debate due to the lack of complete knowledge about the properties of their populations, and their relation to those of galaxies. An increase in the total luminosity of HMXB populations with increasing star formation rate (SFR) and decreasing metallicity has been consistently reported (Kaaret et al. 2011; Brorby et al. 2014; Douna et al. 2015; Ponnada et al. 2020). The former trend is expected as at higher SFR more binaries are created, but it is unclear if the latter is driven by an increase in the number of HMXBs or their individual luminosities.

Although the aforementioned issue has been explored using both semiempirical (e.g., Douna et al. 2015) and population synthesis models (e.g. Lehmer et al. 2021), it is still open mainly because the data are still scarce and highly uncertain, and there is no *ab initio* model for predicting the luminosity of a HMXB.

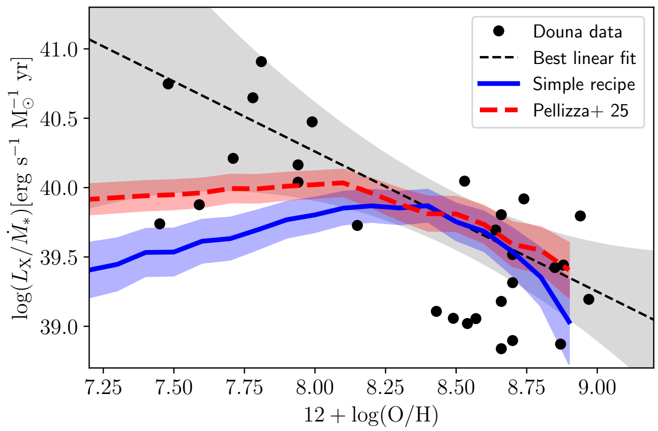

Figure 1. X-ray luminosity per unit SFR vs. metallicity. The prediction of population synthesis models with the simple recipe quoted in the text and the unsteady disk model of Pellizza et al. (2025) are compared to the data compiled by Douna et al. (2015). Shaded regions show 68% confidence levels.

Usually the latter problem is circumvented by using a simple recipe in which the system radiates a fraction of the available accretion power, $L = \eta G M \dot{M}/R$, where L is the X-ray luminosity, G the gravitational constant, $\dot{M}$ the accretion rate, and M and R the mass and radius of the accretor, respectively. This approach encodes all the ignorance about the emission mechanism in the efficiency η, which is assumed to be constant and of the order of 0.1 (e.g., Vivanco Cádiz et al. 2024).

The recipe described above is appealing because it is simple enough to be wired into population synthesis models and cosmological simulations. However, it does a poor job in describing the metallicity dependence of local HMXB populations. A more detailed model was put forth by Pellizza et al. (2025), in which the emission of an unsteady, thin Keplerian accretion disk is computed, and its duty cycle taken into account. This model improves the prediction of the metallicity dependence, as shown in Fig. 1. In this work, we explore the ability of the model of Pellizza et al. (2025) to describe the HMXB host galaxies in the Local Universe. We use the large cosmological hydrodynamical simulation of galaxy formation Eagle (Schaye et al. 2015) and compute, using the unsteady disk model, the HMXB population and luminosities of a set of 1356 galaxies at redshift 0. We use the obtained luminosities to assess the detectability of the galaxies as hosts of HMXBs, and compare the results to the data compiled by Douna et al. (2015). Sect. 2 describes our method; Sect. 3 discusses our preliminary results.

2. Method

We aim to predict the luminosities of HMXB populations in the Eagle simulation. We adopted the galaxy catalogue constructed with the $(25\,\mathrm{cMpc})^3$ simulation vol-

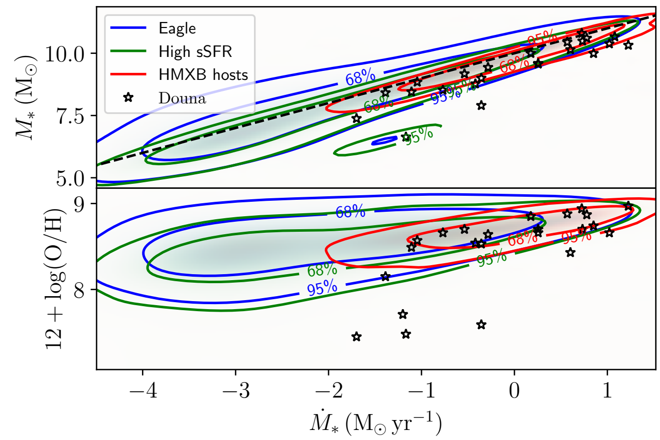

Figure 2. Density of simulated galaxies (shaded colour regions) in the $\dot{M}_* - M_*$ (upper panel) and $\dot{M}_* - 12 + \log(O/H)$ (lower panel) planes, compared to the observed sample of HMXB hosts (black stars). Solid colour contours show the regions enclosing 68 and 95% of the galaxies. The complete simulated population is shown in blue, a sample of it with high sSFR in green, and the HMXB hosts predicted by our model in red. The black dashed line separates low- from high-sSFR systems.

ume, from which we took the SFRs ($\dot{M}_*$), stellar masses (M_*), and metallicities ($12 + \log(O/H)$) of 1356 galaxies. The computation of the HMXB populations and their luminosities follows closely that of Pellizza et al. (2025); we give here only the relevant details. Given the initial mass function of Chabrier (2003), and the binary fraction and secondary mass distributions from Sana et al. (2012), we computed the number of binaries produced in each galaxy in the last 50 Myr, and created by Monte Carlo sampling a zero-age binary population. Assigning a random birth time within the same interval to each binary, we evolved it up to the present using the code SEVN (Iorio et al. 2023) adopting its standard parameters for all physical processes. We selected binaries comprised by a compact remnant (black hole or neutron star) and a non-collapsed star, and computed their individual luminosities L_X as described in Pellizza et al. (2025). Aiming to explore possible biases of the observed sample, we assigned to each Eagle galaxy a probability of being detected as a host proportional to L_X.

3. Results and discussion

Fig. 2 shows the density of simulated galaxies in the $\dot{M}_* - M_*$ and $\dot{M}_* - 12 + \log(O/H)$ planes. The complete Eagle sample of galaxies (in blue in Fig. 2) gives a fair representation of the general galaxy population. This sample follows tight relations between $\dot{M}_*$ and the other variables, extending throughout more than five orders of magnitude in the former. The hosts sample of Douna et al. (2015) has been selected by requiring that galaxies display a large specific SFR (sSFR), $\log(\dot{M}_*/M_\odot\,yr^{-1}) - \log(M_*/M_\odot) > -10$, to avoid contamination of the HMXB population with older X-ray emitting systems, namely low-mass X-ray binaries. The corresponding sample of simulated galaxies is shown in green in Fig. 2, and displays the same tight correlations mentioned above. It is clear from this figure that simulated galaxies occupy in these plots a larger region than the observed sample of HMXB hosts. Galaxies with low SFR and low stellar mass have not been observed as hosts, although they fulfill the high sSFR criterion. However, taking into account the detectability of the hosts determined using the model of Pellizza et al. (2025, in red in Fig. 2) greatly improves the agreement with observations. We conclude that the model of Pellizza et al. (2025) is able to reproduce the observed properties of HMXB hosts at abundances $> 20\%$ solar, suggesting that they are normal galaxies affected by a L_X-dependent bias. This allows a more realistic modelling of HMXB populations to explore their effect on their environment at all redshifts. There are a few observed hosts at low metallicities, which are not predicted by the model, because similar galaxies are absent in the complete Eagle sample. A simulation which better represents low-metallicity galaxies is required to solve this issue.

Acknowledgements. The authors thank financial support from Argentine ANPCyT through grant PICT-2020-0582.

References

Artale, M.C. et al. 2015, MNRAS, 448, 3071
Brorby, M. et al. 2014, MNRAS, 441, 2346
Chabrier, G. 2003, PASP, 115, 763
Douna, V.M. et al. 2015, A&A, 579, A44
Douna, V.M. et al. 2018, MNRAS, 474, 3488
Escobar, G.J. et al. 2021, A&A, 650, A136
Escobar, G.J. et al. 2022, A&A, 665, A145
Fabbiano, G. 2006, ARA&A, 44, 323
Feng, H., Soria, R. 2011, New.Astron.Rev., 55, 166
Fragos, T. et al. 2013, ApJ, 776, L31
Heinz, S., Sunyaev, R. 2002, A&A, 390, 751
Iorio, G. et al. 2023, MNRAS, 524, 426
Kaaret, P. et al. 2011, ApJ, 741, 10
Lehmer, B.D. et al. 2021, ApJ, 907, 17
Mirabel, I.F. et al. 1992, Nature, 358, 215
Mirabel, I.F. et al. 2011, A&A, 528, A149
Pellizza, L.J. et al. 2025, BAAA, 66, 377
Ponnada, S. et al. 2020, MNRAS, 491, 3606
Sana, H. et al. 2012, Science, 337, 444
Schaye, J. et al. 2015, MNRAS, 446, 521
Vivanco Cádiz, F. et al. 2024, BSRSL, 93, 324

ISBN 978-987-24948-9-6